

1 Hourly Assimilation of Different Sources of Observations
2 Including Satellite Radiances in a Mesoscale Convective
3 System Case During RELAMPAGO campaign

4 Paola Belén Corrales^{*a,b,c}, Victoria Galligani^{a,b,c}, Juan Ruiz^{a,b,c}, Luiz
5 Sapucci^f, María Eugenia Dillon^{d,e}, Yanina García Skabar^{d,e,c}, Maximiliano
6 Sacco^d, Craig S. Schwartz^g, Stephen W. Nesbitt^h

7 ^a*Universidad de Buenos Aires, Facultad de Ciencias Exactas y Naturales, Departamento
de Ciencias de la Atmósfera y los Océanos. Buenos Aires, Argentina.*

8 ^b*CONICET – Universidad de Buenos Aires. Centro de Investigaciones del Mar y la
Atmósfera (CIMA). Buenos Aires, Argentina.*

9 ^c*CNRS – IRD – CONICET – UBA. Instituto Franco-Argentino para el Estudio del Clima
y sus Impactos (IRL 3351 IFAECI). Buenos Aires, Argentina.*

10 ^d*Servicio Meteorológico Nacional de Argentina.*

11 ^e*CONICET (Consejo Nacional de Investigaciones Científicas y Técnicas).*

12 ^f*National Institute for Space Research, Brazil, Center for Weather Forecasting and Climate
Studies.*

13 ^g*National Center for Atmospheric Research, Boulder, Colorado.*

14 ^h*Department of Atmospheric Sciences, University of Illinois Urbana-Champaign, Urbana,
Illinois.*

20 **Abstract**

In this paper, we evaluate the impact of assimilating high-resolution surface networks and satellite observations using the WRF-GSI-LETKF over central and north eastern Argentina where the surface and upper air observing networks are relatively coarse. We conducted a case study corresponding to a huge mesoscale convective system (MCS) that developed during November 22, 2018. The accumulated precipitation associated with this MCS was quite high, exceeding 200 mm over northern Argentina and Paraguay. The MCS developed during the Intense Observing Period (IOP) of the RELAMPAGO field campaign. We used the GSI-4DLETKF data assimilation package to

*Corresponding Author

Email address: paola.corrales@cima.fcen.uba.ar (Paola Belén Corrales)

May 16, 2022

produce analyses assimilating observations every hour with 10-km horizontal grid spacing and a 60-member multiphysics ensemble. We conducted four assimilation experiments using different sets of observations: CONV, consisting of conventional observations from NCEP’s prepBUFR files; AWS combining CONV and dense automatic surface weather station networks, SATWND, combining AWS with satellite-derived winds and RAD, including SATWND; and satellite radiances from different microwave and infrared sensors. We found that the assimilation of observations with high temporal and spatial frequency generate an important impact on the PBL, primarily on the precipitable water content, that leads to the development of deep convection and heavy precipitation closer to the observed in this case study. The assimilation of radiance observations produces a better development of the convection mainly during the mature state of the MCS leading to an increase in the accumulated precipitation. We also ran ensemble forecasts initialized from each experiment and evaluated their skill to predict precipitation. We found that the hourly assimilation of the observations in AWS, SATWND, and RAD helped to improve the precipitation forecast.

²¹ *Key words:* Regional Data Assimilation, Surface Observations, Satellite

²² Observations

²³ **1. Introduction**

²⁴ Severe weather events cause significant human and economic losses around
²⁵ the world. A large number of these phenomena are associated with the
²⁶ occurrence of deep moist convection, including tornadoes, intense wind gusts,
²⁷ extreme precipitation in short time periods, large hail, and lightning. Southern

28 South America has one of the highest frequencies in the world of favorable
29 conditions for high-impact meteorological events (Brooks et al., 2003) and
30 large hail events (Cecil and Blankenship, 2012), particularly during austral
31 spring and summer. This is also confirmed by observational evidence and
32 high impact weather reports (Matsudo et al., 2015; Rasmussen et al., 2014).
33 Recently, the RELAMPAGO-CACTI field campaign (Nesbitt et al., 2021) has
34 been conducted to investigate the mechanisms for convective initiation and
35 the occurrence of high-impact weather events associated with deep convection
36 in central Argentina.

37 Forecasting mesoscale meteorological phenomena and particularly deep
38 moist convection is a scientific and technological challenge due to its limited
39 predictability and the difficulties in diagnosing the state of the atmosphere at
40 small spatial and short temporal scales (for example from 1 to 10 kilometers
41 and on the order of minutes). Mesoscale data assimilation (DA) is an approach
42 that can provide appropriate initial conditions for high-resolution numerical
43 forecasts (Sun et al., 2014) and thus has received increasing attention in the
44 last decades.

45 For DA methods to be successful, observing networks with sufficient
46 temporal and spatial resolution capable of capturing mesoscale variability
47 should be used.

48 In that regard, several authors investigated the impact of assimilating
49 surface weather data (e.g. Wheatley and Stensrud (2010), Ha and Snyder
50 (2014), Chang et al. (2017), Bae and Min (2022), Banos et al. (2021),
51 Maejima et al. (2019), and Chen et al. (2016)) using different assimilation
52 methodologies. Most of these studies reported the beneficial impacts of

53 assimilating temperature and dew point observations upon the planetary
54 boundary layer structure and the location and timing of precipitating systems.
55 Sobash and Stensrud (2015) showed using a mesoscale DA system, that the
56 positive impact upon convection initiation and the short range precipitation
57 forecast is achieved if data is assimilated frequently (in the order of minutes,
58 rather than in the order of hours). More recently, Gasperoni et al. (2018)
59 evaluated the impact of assimilating observations produced by private weather
60 station networks which are not incorporated in the operational analysis. They
61 found a positive effect of these observations upon the initiation of deep moist
62 convection. This result is particularly important for data sparse regions such
63 as Southern South America, where operational networks are not dense enough
64 to capture mesoscale details.

65 The impact of other types of high spatial and temporal resolution observa-
66 tions, such as atmospheric motion vectors (AMVs), has also been investigated
67 in the context of limited-area mesoscale DA. Many studies have focused on
68 the impact of these observations on the prediction of tropical storms (e.g.,
69 Wu et al. (2014), Cherubini et al. (2006), and Sawada et al. (2019), among
70 many others). Most of these studies reported an overall positive impact of the
71 assimilation of AMVs for this type of storm. However, some works indicated
72 mixed impacts (e.g. Sawada et al. (2019) reported an improvement in the
73 forecast of the track of the storm but a degradation in the forecast intensity).
74 As stated in J. Zhao et al. (2021a) and J. Zhao et al. (2021b), the impact
75 of assimilating these data on high impact weather events associated with
76 mid-latitude deep convection over land has received relatively less attention.
77 J. Zhao et al. (2021a) and J. Zhao et al. (2021b) assimilated GOES-16

78 AMVs into a storm-scale three-dimensional variational DA system during
79 three high impact weather events. They reported positive impacts of AMVs
80 on the characterization of the storm environment and improved short range
81 precipitation forecasts. Otsuka et al. (2015) and Mallick and Jones (2020)
82 found a slight improvement in the short-range precipitation forecast due to
83 the storm-scale assimilation of high frequency AMVs.

84 While the assimilation of radiance observations into global models is well
85 established (Eyre et al., 2020), the direct assimilation of radiance data into
86 regional models, however, still remains a challenge due to the sparse data
87 coverage, bias correction, and the relatively low model tops used for this
88 application. Bao et al. (2015) studied the impact of assimilating microwave
89 and infrared radiance data on temperature and humidity forecasts over the
90 western USA and found a reduction in the temperature bias at low and
91 mid-levels as a result of the microwave observations but an opposite effect
92 for infrared data. More recently, Zhu et al. (2019) studied the impact of
93 assimilating satellite radiance data within a frequently updated regional
94 system and showed an improvement for all variables, in particular for relative
95 humidity at upper levels. Wang and Randriamampianina (2021) studied the
96 impact of assimilating radiances in the high-resolution Copernicus European
97 Regional Reanalysis. They reported that satellite radiance observations had a
98 neutral impact on the analyses of geopotential height in the lower troposphere,
99 while a slightly negative impact on the upper troposphere and the stratosphere.
100 They also observed similar results for 3-h forecasts initialized from the analysis
101 but a positive impact on 12 and 24 -h forecasts. Given these mixed results,
102 there is still room to analyze the utility of assimilating radiance observations

103 in a limited-area DA system over land. Moreover, to the best of our knowledge,
104 there are no studies related to the direct assimilation of radiance observations
105 over South America.

106 In particular, in South America, the relatively scarcity of conventional
107 observations such as radiosondes increases the potential impact of the ob-
108 servation sources previously discussed. Previous work has shown promising
109 results of mesoscale DA in South America using some of the above mentioned
110 data sources (e.g. Dillon et al., 2016, 2021; Goncalves de Goncalves et al.,
111 2015). In particular Dillon et al. (2021) assimilated high resolution surface
112 weather station networks, GOES-16 AMVs, and satellite temperature and
113 moisture retrievals with promising results. However, no work has been con-
114 ducted yet over this region to investigate the potential contribution of the
115 datasets discussed above. The main objective of this work is to contribute to
116 the quantification and comparison of the impact of high resolution surface
117 weather stations, AMVs, and clear-sky satellite radiances, into a mesoscale,
118 frequently-updated ensemble-based DA system. In particular, we will focus
119 on the impact in the context of mid-latitude mesoscale convective system
120 events. Another particular goal of this paper is to investigate the impact of
121 these data sources in a region where the conventional observation network
122 is rather sparse and where the potential contributions of these observing
123 systems is larger.

124 To reach this goal, we conduct several DA experiments for a case study of
125 a large Mesoscale Convective System (MCS) that developed over Southern
126 South America during Nov 22-23, 2018 during the intense observation period
127 (IOP) of the RELAMPAGO field campaign.

128 The paper is organized as follows. The DA system, the experimental
129 design, and the observations used are presented in section 2. Results are
130 discussed in section 3 and finally, conclusions are summarized in section 4.

131 **2. Data and Methods**

132 *2.1. Case Study*

133 On Nov 22, 2018 a cold front crossed the center of Argentina triggering
134 isolated convective cells that rapidly grew upscale into an exceptionally large
135 MCS. To the north of the region, a warm front contributed to the development
136 of isolated multicells that ultimately grew and merged with the MCS. The
137 MCS traveled approximately 2500 km from south to north, dissipating over
138 Paraguay and Southern Brazil after 42 hours.

139 *2.2. Data assimilation system configuration*

140 The model simulations for the case study are performed using version
141 3.9.1 of the non-hydrostatic Advanced Research version of the Weather Re-
142 search and Forecasting (WRF-ARW, Skamarock et al. (2008)) model. The
143 horizontal grid spacing is 10 km (150 x 200 grid points) in the horizontal
144 and 37 levels in the vertical with the top of the model at 50 hPa. The
145 initial and boundary conditions are provided by the Global Forecast System
146 (GFS) analysis (0.25° horizontal grid spacing and 6-hour temporal resolution;
147 National Centers for Environmental Prediction, National Weather Service,
148 NOAA, U.S. Department of Commerce (2015)). The domain covers the area
149 indicated in Figure 1 to capture the development of the MCS during the
150 simulated period.

151 The analyses are generated using the LETKF implementation (V1.3,
152 Hunt et al. (2007)) part of the Gridpoint Statistical Interpolation analysis
153 system (GSI V3.8; Shao et al. (2016)). A rapid update cycle approach
154 is implemented with hourly analysis and a centered assimilation window,
155 meaning that all the observations within \pm 30 minutes of the analysis time
156 are assimilated. Observations are assimilated in a 4D approach by comparing
157 them with the corresponding first guess state at 10-minute intervals. For
158 radiance observations, the Community Radiative Transfer Model version 2.3
159 (CRTM; Han et al. (2006)) is used as an observation operator to calculate
160 model-simulated brightness temperatures.

161 We use a 60-member ensemble where the ensemble mean at the beginning
162 of the DA cycle is initialized using the GFS deterministic analysis with random
163 perturbations to generate the initial ensemble perturbations. The perturba-
164 tions are generated as scaled differences between two random atmospheric
165 states obtained from the Climate Forecast System Reanalysis (CFSR) data
166 with 0.5° horizontal grid spacing with a smooth time evolution as in Necker
167 et al. (2020) and Maldonado et al. (2021). In this way, we preserved the
168 nearly hydrostatic and geostrophic equilibrium of larger scales. This method
169 helps to prevent an underestimation of the ensemble spread (Ouaraini et al.,
170 2015), and the random perturbations are also applied at the boundaries to
171 maintain proper levels of ensemble spread within the domain.

172 In addition to random perturbations at the lateral boundaries, a multi-
173 physics scheme is used to better represent the uncertainty in model formulation
174 within the DA system. We use 9 different model configurations consisting of
175 the combination of 3 moist convection schemes (Kain–Fritsch (Kain, 2004),

176 Grell–Freitas (Grell and Freitas, 2013), and Betts–Miller–Janjic (Janjić, 1994))
177 and 3 planetary boundary layer schemes (Yonsei University Scheme (Hong,
178 Noh, et al., 2006), Mellor–Yamada–Janjic Scheme (Janjić, 1994), and Mellor–
179 Yamada Nakanishi Niino (Nakanishi and Niino, 2009)). All ensemble members
180 use the same land-surface model (Noah-MP, Chen and Dudhia (2001)), mi-
181 crophysics (WRF single-moment 6-class scheme (Hong, Kim, et al., 2006)),
182 and radiation processes (RRTMG shortwave and longwave scheme (Iacono et
183 al., 2008)) parameterizations.

184 To reduce the effect of spurious correlations in the estimation of error
185 covariances, we use a horizontal localization radius of 180 km and a vertical
186 localization radius of 0.4 (in log pressure coordinates) as in Dillon et al. (2021)
187 for all types of observations. A relaxation-to-prior inflation (Whitaker and
188 Hamill, 2012) is applied with an inflation parameter $\alpha = 0.9$ to mitigate the
189 impact of sampling errors and to consider model errors not accounted for by
190 the multi-model ensemble approach.

191 *2.3. Observations*

192 *2.3.1. Conventional*

193 The conventional observations used are part of the Global Data Assimila-
194 tion System (GDAS) data stream. We assimilated conventional observations
195 included in the Binary Universal Form for Representation of Meteorological
196 Data (PREPBUFR) files generated at the National Centers for Environmental
197 Prediction (NCEP). These consist of surface observations from 117 Conven-
198 tional Surface Weather Stations (CSWS), ships, and upper-air observations
199 from 13 radiosondes sites and aircraft. The orange triangles in Figure 1a
200 indicate the location of the surface stations included in this experiment. The

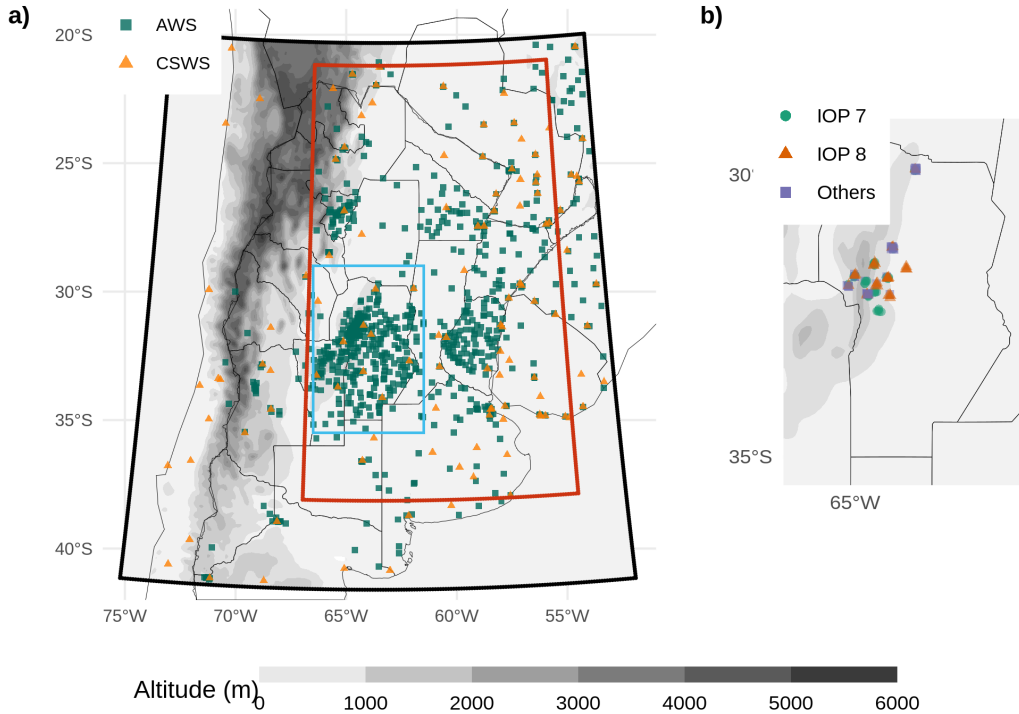


Figure 1: a) The domain used for the simulations (black box), the inner domain used for the experiment comparison (red box), the region shown in b) (light blue box), and the locations of Automatic Weather Stations (AWS, green squares) and Conventional Surface Weather Stations (CSWS, orange triangles). b) Locations of radiosonde launches during RELAMPAGO. Green dots correspond to radiosondes launched during IOP 7, orange triangles are radiosondes launched during IOP 8, and purple squares are radiosondes launched outside the IOP missions. The topography in meters is also shown (shaded).

frequency of these observations varied between 1 hour for surface stations and 12/24 hours for radiosondes. Wind surface observations over oceans (AS-CATW) come from scatterometers and are also included in the PREPBUFR files.

Table 1 lists all the observation types (i.e., surface pressure, temperature, specific humidity, and wind) available for each source, together with their associated errors. The observation errors were specified following the GSI default configuration. In some cases, the error varies with height and depends on the specific platform (aircraft and satellite-derived wind). In terms of quality control, a gross check was performed by the observation operator by comparing the innovation (the difference between the observation and the model-simulated observation based on the first-guess) with a predefined threshold that depends on the observation error (also included in Table 1).

2.3.2. AWS networks

We also assimilate data from 866 Automatic Weather Stations (AWS) that are part of 17 public and private surface networks over Southern South America. The dataset used in this study has been obtained from the RE-LAMPAGO Data Set repository (Garcia et al., 2019). These stations are indicated as green squares in Figure 1a. They have higher spatial coverage than the CSWS and a sampling frequency of 10 minutes in most cases. All stations measure temperature, but only 395 stations provide humidity, 422 provide pressure, and 605 provide wind information. Observation errors used to assimilate these observations are the same as for the CSWS (see Table 1).

224 *2.3.3. Satellite derived winds*

225 Satellite-derived wind observations are also included in the PREPBUFR
226 files available every 6 h, and consist of estimations from GOES-16 (using
227 the visible, infrared, and water vapor channels) and METEOSAT 8 and 11
228 (using the visible and water vapor channels). Due to the domain covered by
229 each of these satellites, GOES-16 is the primary source of satellite-derived
230 winds (99 % of the observations). Observation errors used to assimilate these
231 observations are indicated in Table 1.

232 *2.3.4. Satellite radiances*

233 Satellite radiances available through the GDAS data stream, consisting of
234 infrared and microwave observations, are used in this study. This includes
235 the Advanced Microwave Sounding Unit - A (AMSU-A), Microwave Humid-
236 ity Sounder (MHS), and 2 multispectral sensors; the Atmospheric Infrared
237 Sounder (AIRS) and the Infrared Atmospheric Sounding Interferometer (IASI)
238 over several satellite platforms (see Table 2). Since the regional domain is
239 located in the mid-latitudes and the satellite platforms of interest are on polar
240 orbits, each sensor scans the area only twice a day with a spatial coverage
241 depending on the satellite swath. For this reason, the number of satellite
242 observations varied significantly among cycles. In particular, the multispectral
243 sensors provided between 100 and 1000 observations for every scan every
244 12 hours, contributing 88 % of the total amount of assimilated radiances
245 in our experiment. The vertical location of each radiance observation was
246 estimated as the model level at which its weighting function was maximized as
247 calculated by CRTM. The multispectral sensors have good vertical coverage
248 and are able to sense from the lower troposphere up to the lower stratosphere.

Table 1: Characteristics of the assimilated observations: The code for each observation type and its source, the available variables, the observation error, and the gross check thresholds used.

Code	Platform	Variable	Error	Gross check
CSWS AWS	Surface weather stations	Pressure	1-1.6 hPa^*	3.6 hPa
		Temperature	1.5 K	7 K
		Specific humidity	20 %	8 gKg^{-1}
		Wind	2.2 ms^{-1}	6 ms^{-1}
ADPUPA	Radiosondes	Pressure	1.1-1.2 hPa^{**}	4 hPa
		Temperature	0.8-1.5 K^*	8 K
		Specific humidity	20 %	8 gKg^{-1}
		Wind	1.4-3 $ms^{-1}*^*$	8 ms^{-1}
AIRCFT	Aircrafts	Temperature	1.47-2.5 K^+	7 K
		Wind	2.4-3.6 $ms^{-1}+^+$	6.5-7.5 $ms^{-1}+^+$
ASCATW	Advanced Scatterometers	Wind	1.5 ms^{-1}	5 ms^{-1}
SFCSHP	Ships and Buoys	Pressure	1.3 hPa	4 hPa
		Temperature	2.5 K	7 K
		Specific humidity	20 %	8 gKg^{-1}
		Wind	2.5 ms^{-1}	5 ms^{-1}
SATWND	Satellite-derived winds	Wind	3.8-8 $ms^{-1}*+^+$	1.3-2.5 $ms^{-1}+^+$

* Observation error varied with height.

** Observations above 600 hPa are rejected.

+ Observation error depends on the report type.

249 The channels accepted for assimilation and their associated errors were
250 defined taking into account the low model top (50 hPa). The data preprocess-
251 ing, which is an essential step in the assimilation of radiances, was performed
252 within the GSI system for each sensor specifically. First, a spatial data
253 thinning is applied using a 60 km grid following Singh et al. (2016), Jones et
254 al. (2013), and Lin et al. (2017), where the observations to be assimilated
255 are chosen based on their distance to the model grid points, the observation
256 quality (based on available data quality information), and the number of
257 available channels (from the same pixel and sensor) that passed the quality
258 control. Also, observations over the sea are preferred to those over land or
259 snow (Hu et al., 2018).

260 The thinned observations were then bias corrected. The bias correction
261 (BC) has an air-mass dependent and an angle-dependent component (Zhu
262 et al., 2014) and it is calculated as a multi-linear function of N predictors
263 $p_i(x)$, with associated coefficients β_i . Then, the bias corrected brightness
264 temperature (BT_{bc}) can be obtained as:

$$BT_{bc} = BT + \sum_{i=0}^N \beta_i p_i(x)$$

265 GSI has a constant offset bias correction term ($p_0 = 1$) and the remaining
266 predictors are the cloud liquid water content (CLW), the temperature lapse
267 rate at the pressure of maximum weight, the square of the temperature lapse
268 rate at the pressure of maximum weight, and the emissivity sensitivity. Scan
269 angle-dependent bias is modeled as a 4th-order polynomial (Zhu et al., 2014).

270 In the GSI system, the β_i coefficients are trained using a variational
271 estimation method which solves the β_i that provides the best fit between the

272 simulation and the observations. The coefficients were initialized at 18 UTC
273 Nov 18, 2018 with the GFS system coefficients. The assimilation system was
274 configured to use a constant background error variance of 0.01 to avoid large
275 adjustments in the estimated coefficients at each time.

276 In our experiments, only clear-sky observations are used. For microwave
277 radiances, observations potentially contaminated by clouds are detected using
278 the scattering and Liquid Water Path (LWP) indexes (Weston et al., 2019;
279 Zhu et al., 2016). For the infrared channels, cloud contaminated observations
280 are detected using the transmittance profile calculated within the CRTM
281 algorithms. Additionally, the GSI quality control for infrared sensors looks
282 for observations over water with a large zenith angle (over 60°) to reject
283 channels near the visible range that can be contaminated with reflection. It
284 also performs an emissivity check for observations over land for both infrared
285 and microwave radiances.

286 *2.3.5. Validation dataset*

287 To evaluate the performance of the ensemble-based DA system presented
288 in this article, we use the following observational datasets:

- 289 • The Multi-Network Composite Highest Resolution Radiosonde Data
290 (Earth Observing Laboratory, 2020) from the RELAMPAGO field cam-
291 paign database consisting of high-resolution radiosondes launched from
292 several locations during the IOPs along with the operational radiosondes.
293 Only the soundings that did not enter the assimilation system were
294 used for validation. The experiment period covers IOP missions 7 and
295 8, during which 74 radiosondes were launched in a small area near the

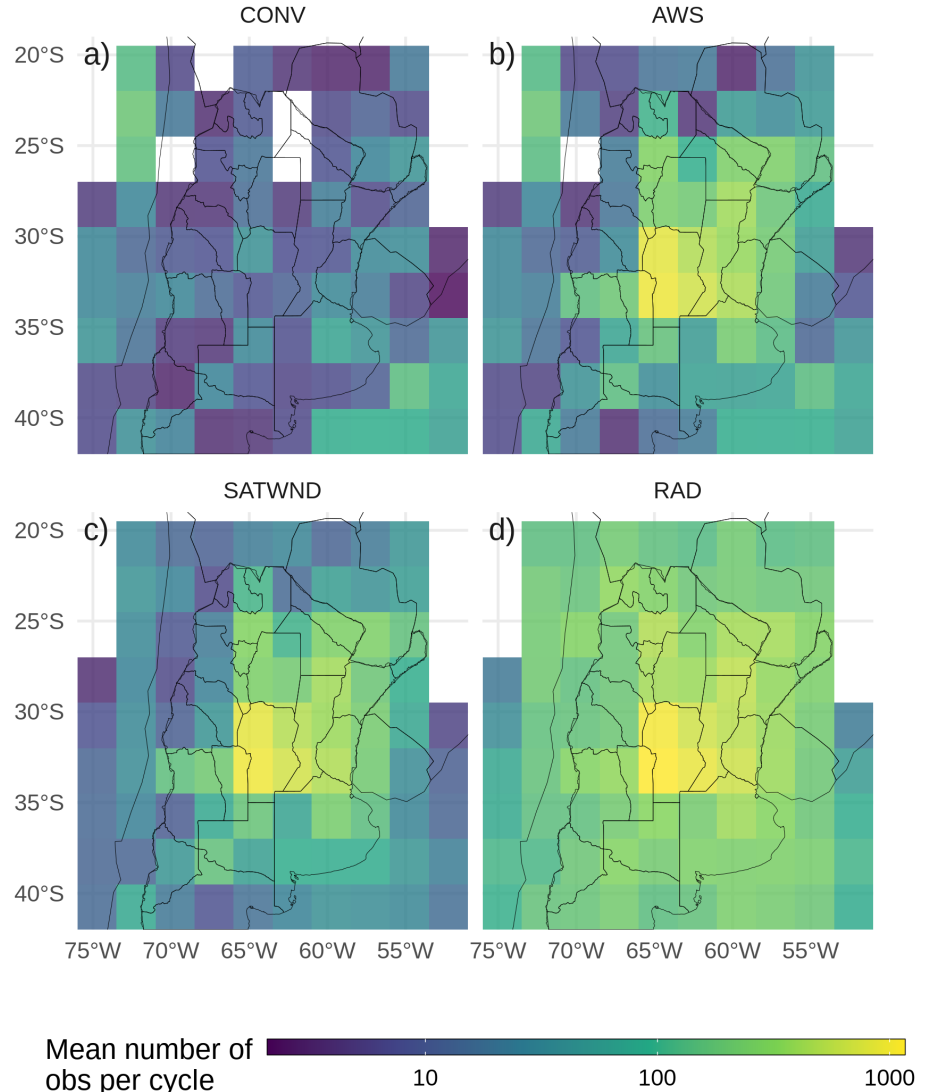


Figure 2: Horizontal spatial distribution of the mean available observations per analysis cycle for the a) CONV, b) AWS, c) SATWND, and d) RAD experiments calculated over 2.5° boxes.

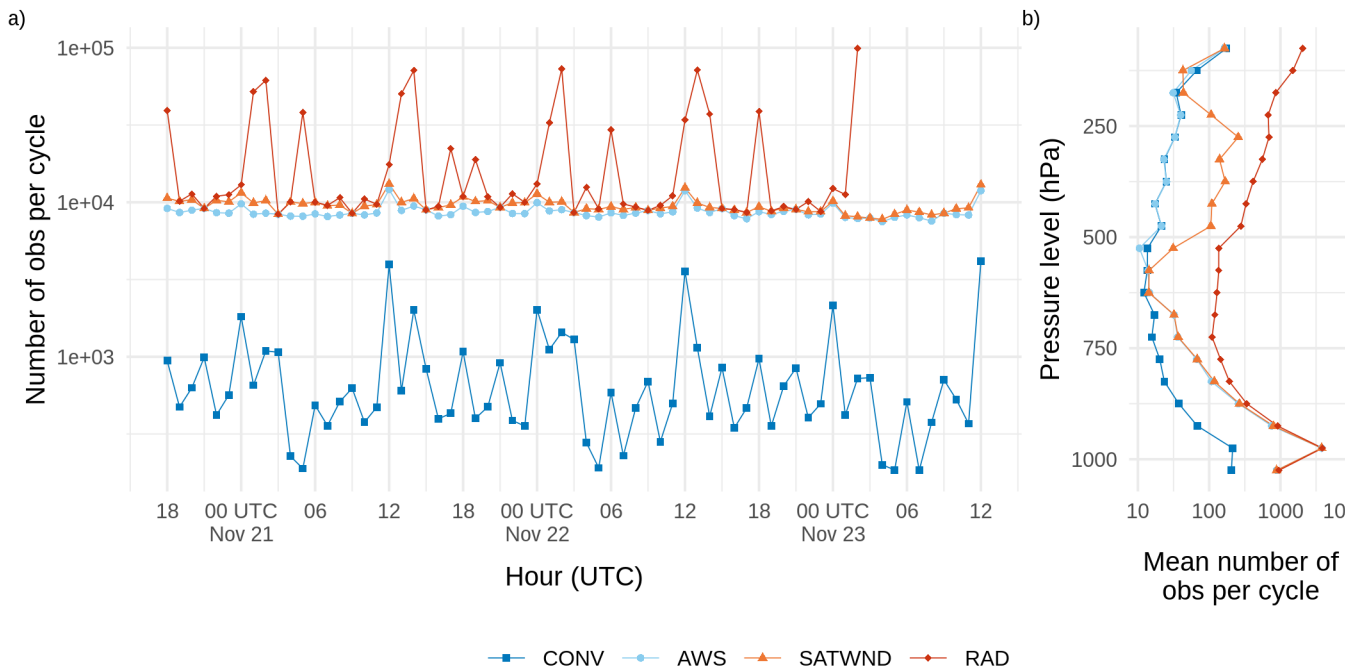


Figure 3: a) Number of assimilated observations per cycle and b) time averaged number of assimilated observations per cycle divided into 50 hPa-depth vertical layers for the CONV (blue squares and line), AWS (light blue dots and line), SATWND (orange triangles and line) and RAD (red diamonds and line) experiments.

Table 2: List of the available sensors over several platforms, the number of accepted channels for the assimilation, and the percentage of assimilated observations calculated over all radiance observations and all cycles.

Sensor	Platform	Assimilated channels	Percentage over total
AIRS	AQUA	52	31.63 %
AMSUA	NOAA15	2	3.31 %
	NOAA18	2	4.45 %
	METOP-A	2	2.08 %
IASI	METOP-A	66	52.72 %
	METOP-B	68	3.47 %
MHS	NOAA19	2	0.68 %
	METOP-A	3	0.8 %
	METOP-B	3	0.85 %

296 center of the experimental domain (Figure 1b).

- 297 • The Satellite precipitation estimation IMERG Final Run with 0.01°
 298 spatial resolution and 30 minutes temporal resolution (Huffman et al.,
 299 2018) was used as a reference state to validate the skill of 1-hour forecasts
 300 to represent the precipitation over the domain.
- 301 • Radar observations are used to perform a qualitative and visual as-
 302 sessment of the convective features. The data comes from 9 radars
 303 located in the domain and is provided by the Argentine C-band Doppler
 304 dual-polarization weather radar network (de Elía et al., 2017) with a
 305 temporal frequency of 10 minutes. For this work, only the maximum
 306 reflectivity in the column (COLMAX) closest to the analysis time was

Table 3: Observation types assimilated in each experiment.

Obs type	CONV	AWS	SATWNDRAD
Conventional (PREPBUFR)	x	x	x
Conventional (AWS)		x	x
Satellite-derived winds		x	x
Radiances			x

307 used.

308 *2.4. Experimental design*

309 To investigate the impact of different observations upon the analysis, four
 310 DA experiments were performed using different observation sets (Table 3).
 311 The CONV experiment uses only conventional observations from PREPBUFR.
 312 In a second experiment, referred to as AWS, we assimilate all the observations
 313 included in CONV plus the 10-minute frequency surface observations from
 314 AWS. In the third experiment, referred to as SATWND, we assimilate all the
 315 observations of the AWS experiment and the satellite-derived winds. Finally,
 316 a fourth experiment referred to as RAD assimilates all available clear-sky
 317 radiances from sensors onboard polar orbiting satellites as described in section
 318 2.3.4.

319 The horizontal distribution of the average number of assimilated observa-
 320 tions per cycle in each experiment is shown in Figure 2. The larger number of
 321 assimilated observations over the center and east of the domain corresponds

322 to the AWS observations. In Figure 3a the number of assimilated observations
323 over time is shown. Local maxima at 12 and 00 UTC found mainly in CONV
324 are attributed to operational soundings. The strong variability in the number
325 of radiance observations per cycle is also noticeable and depends on the satel-
326 lite coverage. The maxima at 13-14 and 01-02 UTC in RAD correspond to
327 the contribution of the multispectral sensors. The vertical distribution of the
328 mean number of observations per cycle (Figure 3b) shows a maximum in low
329 levels due to the AWS observations. Satellite-derived winds are maximized at
330 the upper troposphere (between 500-250 hPa). Above 850 hPa, most of the
331 observations correspond to radiance observations.

332 All the assimilation experiments start at 18 UTC Nov 20, 2018 and
333 continue until 12 UTC Nov, 23 (totaling 67 hours/assimilation cycles). The
334 initial 60-member ensemble is generated as explained in section 2.2 from a
335 spin-up run without assimilating observations performed between 12 UTC
336 and 18 UTC Nov, 20 (Figure 4).

337 Ensemble forecasts initialized from the different analysis experiments at
338 00 and 06 UTC Nov 22 were performed to evaluate the impact of the different
339 observing networks on short range precipitation forecasts. Both forecasts
340 are integrated until 12 UTC Nov 23. All forecasts use the same domain and
341 ensemble configuration as the analysis. The boundary conditions for the
342 ensemble members are generated by adding random perturbations to the GFS
343 deterministic forecast (0.25° horizontal grid spacing and 6-hour temporal
344 resolution; National Centers for Environmental Prediction, National Weather
345 Service, NOAA, U.S. Department of Commerce (2015)).

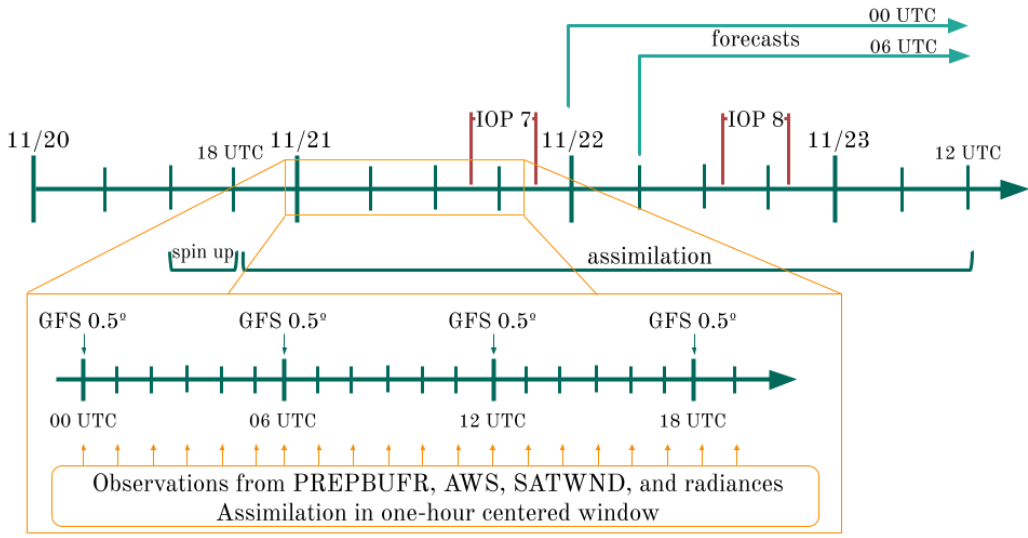


Figure 4: Figure 4. Diagram of the analysis cycles between 18 UTC Nov 20, and 12 UTC Nov 23 plus spin up period of 6 hours. The zoomed section shows the hourly assimilation that is performed within a one-hour centered window and new boundary conditions from GFS every 6 hours. The two IOP missions from the RELAMPAGO field campaign and the ensemble forecast initialized at 00 and 06 UTC Nov 22 are shown.

346 2.5. Verification methods

347 A set of metrics are selected to evaluate different aspects of the analysis
348 obtained in the experiments conducted in this paper. These aspects include
349 a validation of how the uncertainty is quantified in the first-guess and in the
350 analysis, and how different experiments fit an independent set of observations
351 that are not assimilated.

352 To evaluate the consistency of the uncertainty quantification in the first-
353 guess and in the analysis we use the Reduced Centered Random Variable
354 (RCRV, Candille et al. (2007)) which is defined as:

$$RCRV = \frac{x_o - m}{\sqrt{\sigma_o^2 + \sigma^2}}$$

355 where x_o is the assimilated observation and its error σ_o , the ensemble
356 mean of the analysis in observational space m , and the standard deviation σ
357 of the ensemble. The average of $RCRV$ computed over all the realizations
358 represents the bias of the ensemble mean with respect to the observations
359 normalized by the estimated uncertainty:

$$meanRCRV = E[RCRV]$$

360 The standard deviation of the $RCRV$ or $sdRCRV$ measures the agreement
361 of the ensemble spread and the observational error with respect to the distance
362 between the ensemble mean and the observations, and then the systematic
363 over- or under- dispersion of the ensemble:

$$sdRCRV = \sqrt{\frac{M}{M-1} E[(RCRV - meanRCRV)^2]}$$

364 where M is the ensemble size. A consistent system will have no bias
 365 ($meanRCRV = 0$) and a standard deviation equal to 1 ($sdRCRV = 1$).
 366 If the ensemble has a positive bias, $meanRCRV$ will be positive, on the
 367 opposite, if the ensemble has a negative bias, $meanRCRV$ will be negative.
 368 A $sdRCRV > 1$ () indicates that the ensemble is underdispersive and an
 369 $sdRCRV < 1$ indicates that the ensemble is overdispersive.

370 The fit of the first-guess and analysis to a set of independent observations,
 371 the high-resolution radiosondes from RELAMPAGO, is computed based on
 372 the Root Mean Square Error (RMSE) and the BIAS:

$$RMSE = \sqrt{\frac{1}{N} \sum_{i=1}^N (X_i - O_i)^2}$$

$$BIAS = \frac{1}{N} \sum_{i=1}^N (X_i - O_i)$$

373 where O and X stand for independent observations and the simulations
 374 respectively, and N is the sample size.

375 For the comparison of the first-guess precipitation with the IMERG
 376 precipitation estimates, we compute the Fractions Skill Score (FSS, Roberts
 377 (2008)) for different neighborhood length scales and thresholds:

$$FSS = 1 - \frac{\sum_{i=1}^N (P_{xi} - P_{oi})^2}{\sum_{i=1}^N (P_{xi})^2 + \sum_{i=1}^N (P_{oi})^2}$$

378 where P_{oi} is the fraction of grid points in the i -th sampling area in which
 379 the observed accumulated precipitation is greater than a specified threshold.
 380 Following Roberts et al. (2020), P_{xi} is calculated from the ensemble probability
 381 precipitation over the same threshold in each grid point by averaging over

382 the i -th sampling area. The FSS was computed from the accumulated
383 precipitation over 6 hr periods by adding the 1-hr accumulated precipitation
384 forecasts over 6 consecutive assimilation cycles.

385 *2.6. Computation procedures*

386 We performed all the experiments at the National Center for Atmospheric
387 Research (NCAR) supercomputer Cheyenne (Computational and Information
388 Systems Laboratory, 2019). All the analyses in this paper were performed
389 using the R programming language (R Core Team, 2020), using data.table
390 (Dowle and Srinivasan, 2020) and metR (Campitelli, 2020) packages. All
391 graphics are made using ggplot2 (Wickham, 2009) and the paper was rendered
392 using knitr and rmarkdown (Allaire et al., 2019; Xie, 2015).

393 **3. Results**

394 *3.1. Ensemble consistency*

395 To investigate the ability of the first-guess ensemble mean to fit the
396 observations taking into account the uncertainties of the forecast and the
397 observations, we calculated the *meanRCRV* and the *sdRCRV* for the RAD
398 experiment. As this experiment assimilates all types of observations used
399 in this work, it is possible to analyze the consistency of the ensemble by
400 comparing it with each type of observation. Figure 5 shows the *sdRCRV*
401 for surface observations box-averaged to a 2.5° grid. The *sdRCRV* for wind
402 observations (Figure 5a) is close to 1 suggesting a good agreement between
403 the ensemble spread, the forecast error, and the observation error. For the
404 temperature (Figure 5b), the results are similar except that for some areas in

405 the west of the domain the $sdRCRV$ can be as high as 4.5. In this region,
406 the mean innovation was overly large due to the complex terrain leading to
407 large differences between the model topography and the station height.

408 Figure 6 shows the mean and standard deviation of the RCRV for the
409 upper-air observations. Figures 6a-b show the RCRV statistics for sound-
410 ings (ADPUPA) and aircraft (AIRCAR and AIRCFT). Both ADPUPA and
411 AIRCFT show a generally good agreement between the ensemble spread
412 and the observation error. As sounding observations and their associated
413 errors are known to be reliable, this result indicates that the ensemble has
414 an appropriate spread. AIRCAR presents an irregular profile with $sdRCRV$
415 values that suggest that the error for this type of observation is overestimated.
416 ADPUPA and AIRCAR present a $meanRCRV$ profile near zero at middle
417 and upper levels but ADPUPA observations show a cold bias with respect to
418 the model at low levels, a characteristic already studied in Ruiz et al. (2010)
419 and Dillon et al. (2021).

420 For satellite-derived winds (Figure 6c) at low levels, where there are not
421 many observations available, the profiles of $meanRCRV$ and $sdRCRV$ show
422 a larger departure from the expected behavior with a negative bias, and a
423 possible overestimation of the observation error. Wind estimations derived
424 from water vapor channels are abundant above 500 hPa where their bias is
425 close to zero. The only exception are the EUMETSAT observations which
426 contribute very little in the region.

427 The mean RCRV profiles calculated from the radiance observations (Figure
428 6d) show almost no bias and the same happens if the $meanRCRV$ is calculated
429 over each channel of each sensor (not shown). This indicates that the bias

430 correction algorithm works as expected. The $sdRCRV$ values are less than 1
431 for all sensors possibly due to an overestimation of the observation errors to
432 reduce the influence of potentially erroneous observations.

433 Overall, these results indicate that the ensemble spread is consistent with
434 the short-range forecast error and that systematic errors are relatively small
435 for most of the observation types used in this work. Moreover, these results
436 suggest the inflation parameter $\alpha = 0.9$ is adequate for the system.

437 *3.2. Impacts of assimilated observations*

438 In this section, we present the impact of assimilating different observation
439 types on variables which are particularly relevant for the occurrence of deep
440 moist convection. The analysis is performed over a smaller domain (red
441 box in Figure 1a) to focus on the region most directly affected by the MCS.
442 Figures 7a-c show the analysis difference between experiments in the spatially
443 averaged vertical profile of temperature. By averaging the differences between
444 two experiments we can isolate the systematic impact produced by different
445 observing systems on the analyzed state. During the first day, the assimilation
446 of AWS observations results in a colder PBL. This cooling effect has a clear
447 diurnal cycle, being stronger during nighttime (Figure 7a). During the
448 second day of the experiment, the impact of AWS observations extends into
449 the middle and upper troposphere coinciding with the mature stage of the
450 MCS. The warm difference shown in AWS-CONV between 500 and 200 hPa
451 is produced by the development of stronger convection in AWS compared
452 to CONV. This is a good example of how low-level information provided
453 by surface weather stations can rapidly spread into the troposphere in the
454 presence of deep moist convection. Although the mid-to-upper circulation can

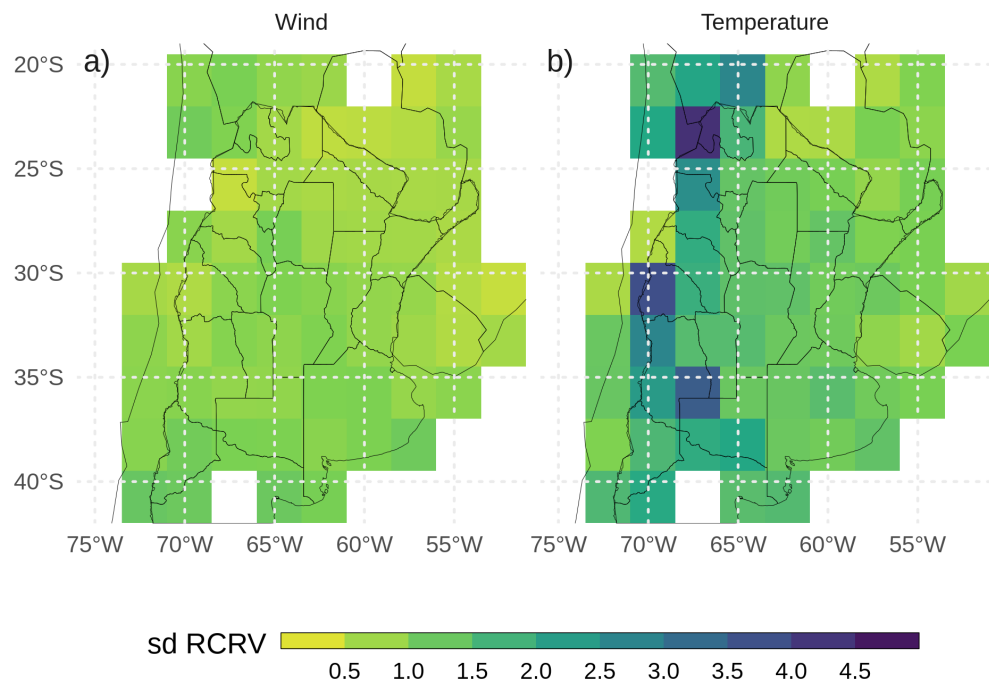
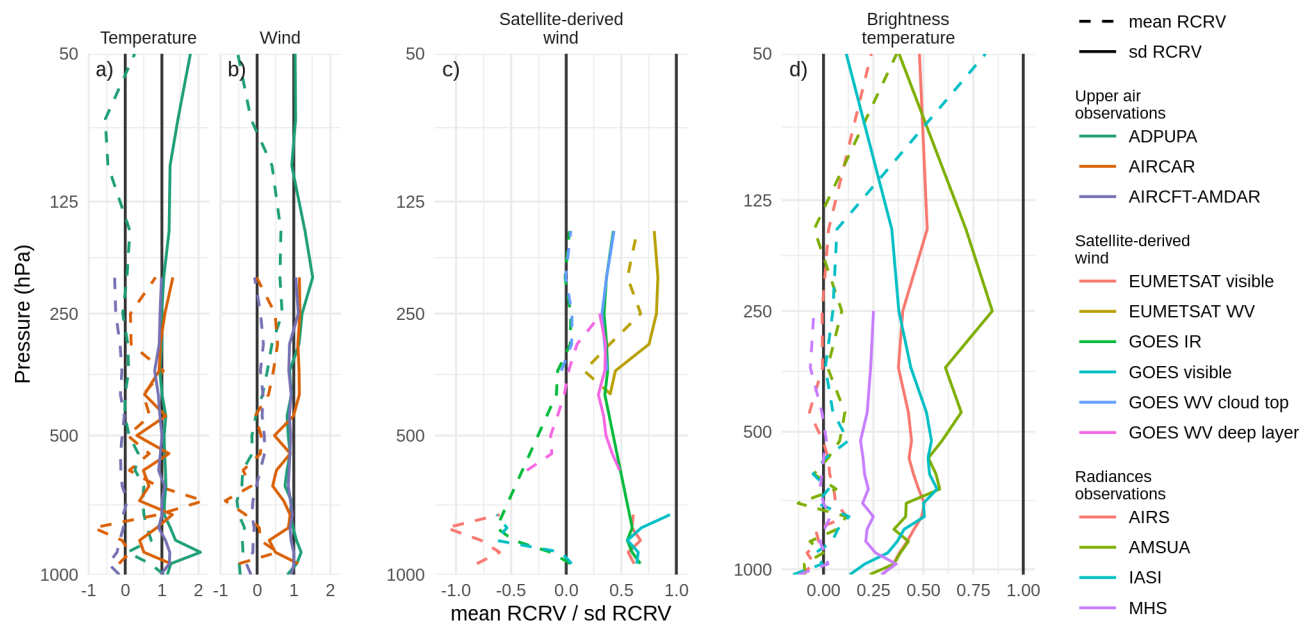


Figure 5: First guess *sdRCRV* calculated for surface observations (from PREPBUFR and AWS) of a) wind, and b) temperature averaged over 2.5° boxes for the RAD experiment. Observations were aggregated every hourly cycle for the entire experiment period.



455 have an important impact on the organization and evolution of the MCS over
456 the region, the satellite-derived winds did not have an appreciable impact
457 on the mean temperature and humidity (Figure 7b-e), possibly due to the
458 large observation errors used for the assimilation. During the first day of the
459 experiment, the assimilation of radiances produces a warming effect in the
460 PBL which partially compensates for the cooling effect of AWS observations
461 (Figure 7c). No clear systematic impact is found above the PBL during this
462 period. During the second day, the impact of radiance observations is found
463 through the troposphere with a distribution that is similar to the impact
464 found in the AWS experiment but with the opposite sign.

465 Comparing the specific humidity in the experiments (Figures 7d-f), the
466 impact of assimilating AWS with fine spatial and temporal resolution is most
467 substantial at low levels (Figure 7d). The PBL in the AWS experiment is
468 consistently moister than in the CONV experiment particularly at nighttime.
469 The increase in low-level moisture by a denser surface network is consistent
470 with previously reported dry biases in the WRF model over the region (Ruiz
471 et al., 2010). We found that the moistening of the PBL is mainly driven
472 by the covariance between temperature and specific humidity within the
473 PBL. In our experiment and over the center of the domain, this covariance
474 remains negative, increasing low-level moisture as the observations introduce
475 negative temperature corrections. As for the temperature, the systematic
476 impact of satellite-derived winds on moisture is small (Figure 7e). Figure 7f
477 shows that radiances reduce low-middle level moisture during the first day of
478 the experiment. The drying effect extends to lower-middle levels during the
479 second day of the experiment coinciding with the development of the MCS

480 between 00 and 12 UTC Nov 22.

481 The impacts on the wind components are shown in Figure 8, along with
482 the corresponding averaged wind component in the experiment with the
483 largest number of assimilated observations (for example, Figure 8a shows the
484 zonal wind difference between AWS and CONV and the zonal wind for AWS).
485 The assimilation of AWS produces a more easterly wind and a less northerly
486 wind at low levels during the first two days of analysis (Figures 8a,b). There
487 is a diurnal cycle in the impact of surface weather stations on the meridional
488 velocity (Figure 8d) with a stronger reduction of the northerly wind during
489 night hours. This indicates that surface observations are reducing the intensity
490 of the low level jet present in the pre-convective environment. After 18 UTC
491 Nov 22, the opposite effect is observed when the MCS is moving through the
492 domain. After the initiation of the convective cells, the systematic impact on
493 the wind field is larger at mid and upper levels (Figures 8d, f). During Nov 22
494 and 23 the impact of assimilating AWS observations produces an increase of
495 northerly wind in upper levels. This could be a consequence of a stronger MCS
496 with an increased polar side upper level outflow. Although satellite-derived
497 wind observations produce the largest impact in mid-to-upper levels where
498 the number of observations is largest; the systematic impact is overall smaller
499 than the one produced by assimilating data from AWS (Figures 8b, e).

500 The assimilation of radiances produces a reduction in the westerly wind
501 compared with respect to SATWIND in low and upper levels (Figure 8c). For
502 the meridional wind, these observations produce an enhancement on average
503 of the northerly low-level flow of $1ms^{-1}$, opposite to what is generated by
504 the assimilation of AWS observations during the nights, between 03 and 12

505 UTC, previous to the development of the MCS (Figure 8f). At upper levels
506 and during Nov 22 and 23 the average impact of assimilating radiances is a
507 decrease in the wind speed. The meridional wind field at 200 hPa at different
508 times shows that the outflow from the MCS is even more intense than in the
509 other experiments, while the southerly wind ahead of the MCS also increases
510 producing an average reduction of the northerly wind (Figure 8f).

511 To investigate how changes in the PBL can modify the pre-convective
512 environment, we compare the horizontal distribution of the low level northerly
513 flow (for the first 7 sigma levels), precipitable water, low level temperature,
514 and CAPE for the analysis at 00 UTC Nov 22 (after 30 assimilation cycles). At
515 that moment the first convective cells were developing over the southern region
516 of the domain along the cold front. Figure 9a shows the precipitable water
517 (shaded) and the vertically averaged low-level meridional wind component
518 (contours). We found that the moist tongue extending over the northern part
519 of the domain is enhanced by the assimilation of denser surface observations.
520 The moisture increase is particularly strong at the southern tip of this tongue,
521 just ahead of the cold front where convection initiation was taking place. AWS
522 and SATWND experiments are very similar, with values of precipitable water
523 over 55 kg m^{-2} north of 30°S and a similar vertical distribution of specific
524 humidity (not shown). RAD has lower precipitable water content than AWS
525 and SATWND, but higher than CONV. The distribution of moisture at low
526 levels in RAD seems to be the result of the combination of the moistening
527 effect of assimilating AWS – partially compensated by the assimilation of
528 radiance observations – and a reduced meridional moisture transport due to
529 the weaker northerly flow over the center of the domain compared to CONV.

530 The analyzed distribution of temperature and moisture in the PBL (Figure
531 9b) resembles the characteristics observed in the temperature profiles (Figure
532 7a-c) where AWS produces a colder PBL than CONV while the PBL in RAD
533 is warmer than in SATWND. On average the PBL in AWS and SATWND is
534 colder than in CONV, while RAD shows a warmer PBL than AWS due to
535 the assimilation of radiance observations. Figure 9c shows the most unstable
536 convective available potential energy (MCAPE, shaded) and the 0 to 6 km
537 wind shear. The values of MCAPE in CONV do not exceed 2000 JKg^{-1}
538 while the rest of the experiments show maximum MCAPE over 4000 JKg^{-1} .
539 MCAPE in the RAD experiment is lower compared to AWS or SATWND. This
540 is consistent with less humidity in the PBL with respect to these experiments
541 but may be partially compensated by a slightly warmer PBL in the RAD
542 experiment. The 0-6 km wind shear is more intense in AWS, SATWND, and
543 RAD reaching values over 15 ms^{-1} at the southern tip of the region with
544 positive MCAPE values. Moreover, in this same region, these experiments
545 show larger MCAPE values than CONV. Note that wind shear over 15 ms^{-1}
546 is associated with the development of more intense and organized MCSs (Chen
547 et al., 2015) and also with conditions favorable for supercells (Markowski and
548 Richardson, 2010).

549 *3.3. Validation against independent observations*

550 First, we analyze the impact of assimilating different observation types in
551 terms of the representation of the MCS and its associated precipitation. Figure
552 10a shows the hourly accumulated precipitation as estimated by IMERG,
553 and the probability matched mean (PM) (Clark, 2017) for the first-guess
554 hourly accumulated precipitation as averaged between 67°W and 54.5°W as

555 a function of time and latitude in the different experiments. The heaviest
556 precipitation (over 12 mmh^{-1}) starts during the afternoon of Nov 22 and
557 continues during Nov 23 after the end of the simulated period (Figure 10a). In
558 all the experiments, the accumulated precipitation in the short-range forecasts
559 is underestimated. This is particularly evident in CONV (Figure 10b), where
560 the convection initiation is delayed and occurs further north with respect to
561 the observed initiation. AWS, SATWND, and RAD better capture the timing
562 and location of convective initiation (Figures 10c-e). AWS and RAD show a
563 more fragmented distribution compared with SATWND, possibly due to the
564 development of less organized convection during Nov 22. After 18 UTC Nov
565 22, RAD shows improvements in the precipitation rate and its distribution
566 compared to the other experiments as a result of enhanced development of
567 the convection.

568 To quantify the spatial match between the observed precipitation and
569 the first-guess hourly accumulated precipitation for the different experiments,
570 we compute the FSS in 6-hour moving windows for different thresholds
571 and spatial scales (Figure 11). All experiments show similar values of FSS
572 during the initiation of the convection before 06 UTC Nov 22 except for
573 RAD which performs better than the rest of the experiments during this
574 period. This indicates that radiance observations have a positive impact on
575 the analysis. The FSS for CONV is the lowest compared to the rest of the
576 experiments and the differences are larger during the mature stage of the
577 MCS. AWS and SATWND show similar FSSs indicating that satellite-derived
578 wind assimilation has little impact on the precipitation for this case study.
579 The assimilation of radiances led to an overall improvement of the 1-hour

580 forecast precipitation, particularly for the 25 mm threshold during the period
581 of heaviest precipitation on Nov 22 (Figure 11b,d). The enhancement is also
582 important at the developing stage of the MCS (between 00 and 12 UTC Nov,
583 22 and also for spatial scales above 500 km, not shown).

584 To complement the analysis, Figure 12 shows the observed maximum
585 reflectivity in the vertical column (COLMAX) and the ensemble mean COL-
586 MAX for the CONV and RAD experiments at different times between 10
587 and 19 UTC Nov 22. These experiments were chosen because they represent
588 the analysis with the minimum (CONV) and maximum (RAD) number of
589 assimilated observations. In addition, they are the worst (CONV) and best
590 (RAD) performing experiments in terms of the 1-hour precipitation forecast
591 skill (Figure 11). Overall, none of the short-range forecasts capture the
592 mesoscale details in the reflectivity distribution. This is partially expected
593 considering the coarse horizontal grid spacing (10 km), which is not enough to
594 appropriately represent the strength of the convective band associated with
595 the MCS. Also, the ensemble mean produces a smoothing effect that reduces
596 the amplitude of local maxima in the forecast reflectivity field. RAD better
597 represents the observed features of the system showing a stronger and more
598 organized MCS than CONV, over the domain center at 10 and 13 UTC (first
599 and second columns in Figure 12). The convective cells that initiate after
600 16 UTC along the warm front in the northeast part of the domain are well
601 captured by both experiments but are better represented in terms of strength
602 in RAD. In addition, CONV captures the location of the MCS, but the
603 convection seems to be less organized and much weaker than in RAD. Before
604 and after the times shown in Figure 12, the agreement between experiment

605 and observations is quite good in the regions where radar data are available,
606 especially for RAD.

607 Finally, Figure 13 shows the RMSE and bias calculated by comparing the
608 experiments with radiosonde data from the RELAMPAGO missions, IOP 7
609 from 15 to 21 UTC Nov 21 (including 30 radiosondes), and IOP 8 from 14 to
610 20 UTC Nov 22 (including 22 radiosondes).

611 IOP 7 (Figures 13a-d) provides a good characterization of the pre-convective
612 environment during the first day of our experiments. The area where the
613 observations were taken was characterized by mostly clear skies and a low-
614 level northerly flow associated with warm and moist advection. In general,
615 the experiments show a similar RMSE and bias for all the variables. AWS
616 observations were able to reduce the RMSE for temperature and dew point
617 temperature in the PBL and reduce a small dry bias. However, AWS degra-
618 dated the zonal wind between 7 and 12 km increasing the bias and RMSE
619 (Figure 13c).

620 For IOP 8 (Figures 13e-h), the densely observed area was behind the
621 MCS, but far enough from it to not be directly affected by its mesoscale
622 circulation. This area was also behind the cold front and affected by low-level
623 cold advection. The assimilation of AWS, SATWND, and RAD reduces
624 the cold bias and RMSE for temperature between 5 and 12 km and the
625 RMSE in the PBL compared with CONV (Figure 13e). The reduction of bias
626 and RMSE is also important for dew point temperature (Figure 13f) with
627 SATWND showing the biggest impact followed by AWS and RAD. The zonal
628 wind is overestimated in the analyses and only RAD shows an improvement
629 with respect to CONV in the upper troposphere (Figure 13g). At low levels

the meridional wind (Figure 13g) presents a negative bias, indicating an underestimation of the southerly wind behind the cold front principally in AWS, SATWND, and RAD. In fact, low level biases in these experiments are higher than in the CONV experiment, indicating a detrimental effect of the additional observations (possibly associated with the effect of AWS).

3.4. Ensemble forecast validation

In this section, we analyze the 60-member ensemble forecast initialized at 00 and 06 UTC Nov 22 from each experiment that runs for 36 and 30 h respectively, until 12 UTC Nov 23. We calculated the FSS for the ensemble forecasts in 6-hour moving windows for the same thresholds and spatial scales as for the first-guess hourly accumulated precipitation to quantify the skill of the forecasts to predict precipitation (Figure 14). CONV forecasts perform very poorly in terms of the FSS compared with the experiments that include other sources of observations. AWS, SATWND, and RAD show improvements in the FSS values, particularly for the higher threshold (Figure 14b, d). Moreover, the late initialization at 06 UTC performs better for AWS, SATWND, and RAD than the forecast initialized at 00 UTC, highlighting the positive impact of the observations assimilated between 00 and 06 UTC.

The satellite-derived wind observations show a clearly positive impact on the forecast, in contrast to what was seen when comparing the 1-h forecast with independent observations in terms of precipitation. Conversely, the radiance observations resulted in a neutral to a slightly negative impact on the forecast as opposed to what was seen when comparing the 1-h forecast to IMERG estimations.

654 **4. Conclusions**

655 In this paper, we investigate for the first time in South America the impact
656 of different observation systems on the performance of an ensemble-based
657 mesoscale regional DA system. In particular, we explore the impact upon the
658 analysis quality of assimilating frequent and relatively dense surface observa-
659 tions, satellite derived winds, and satellite clear-sky radiances from multiple
660 sensors. Southern South America is a particularly interesting region due to the
661 heterogeneity and sometimes coarse resolution of the operational observing
662 network (considering both surface based and upper air observations). This
663 combined with a climatology characterized by frequent organized convective
664 events makes mesoscale DA particularly challenging. To consider these issues,
665 we used a case study approach of a massive mesoscale convective system that
666 developed over Southern South America, particularly in a region where the
667 surface and upper-air observing networks are too coarse to capture variability
668 at the mesoscale and that took place on Nov 22, 2018.

669 We evaluated the consistency of the ensemble using the RCRV calcu-
670 lated for each type of observation used in RAD. Conventional observations
671 including surface data and upper air observations from soundings and aircraft,
672 show a $sdRCRV$ near 1 indicating a good agreement between the ensemble
673 spread and the observational errors with respect to the distance between
674 the ensemble mean and the observations. For satellite-derived winds and
675 radiance observations, the $sdRCRV$ is lower than 1, which could be the result
676 of an underdispersive ensemble or an overestimation of the observation errors.
677 However, taking into account that the observation error for satellite-derived
678 wind is overestimated (to avoid strong impacts on the analysis for poor quality

estimations) and that the results obtained for more reliable observations (such as soundings) were good, we conclude that the ensemble has a reasonable spread.

In terms of the analysis, we found that AWS observations, which have high spatial and temporal resolution, produce impacts throughout the troposphere, especially in the PBL. In particular, the precipitable water content and the low level meridional circulation in the AWS experiment lead to the development of deep convection and heavy precipitation closer to the observed in this case study. We also found positive results when assimilating radiance observations that produce an adequate development of the convection, mainly during the mature stage of the MCS, leading to an increase in the accumulated precipitation compared with the other experiments. However, all experiments underestimated the 1-hour accumulated precipitation when compared to IMERG estimates. While the assimilation of satellite-derived wind does not produce a noticeable impact on the analysis with respect to the AWS experiment, this is possibly due to the small number of observations in low levels available for this case study and its large observation error. However, there are substantial improvements for the accumulated precipitation distribution. A more comprehensive analysis is necessary to assess the possible impacts on middle and upper levels.

Taking advantage of the observations taken during the RELAMPAGO field campaign, we compared the experiments with the soundings launched during IOPs 7 and 8. For the pre-convective environment (IOP 7), we observed an improvement at low levels when assimilating AWS observations for the temperature, dew point temperature, and meridional wind. In particular,

704 AWS observations correct a dry bias already observed by Ruiz et al. (2010).
705 For IOP 8, after the MCS crossed the center of the domain, we found a positive
706 impact in low levels when assimilating more observations for the temperature
707 but the opposite effect for the dew point temperature. In this case, the
708 analyses have a moist bias that increases with the assimilation of AWS and
709 radiance observations. We noted a negative covariance between temperature
710 and moisture content over this region that could lead to a moistening of
711 the PBL. It is not clear what produces these negative covariances but it is
712 evident that the corrections introduced by the observations are degrading the
713 estimation of the moisture content during this period, which requires further
714 analysis.

715 We also analyzed the performance of independent ensemble forecasts ini-
716 tialized from the analyses to forecast the precipitation during Nov 22. The
717 forecast initialized from AWS, SATWND, and RAD are able to forecast the
718 precipitation substantially better than CONV. In particular, the continuous
719 assimilation of satellite-derived wind and radiance observations helps to im-
720 prove the latest initialization but only the satellite-derived wind observations
721 produces a positive impact that persists throughout the forecast.

722 To summarize, in this study we conclude that the assimilation of surface
723 observations with high spatial and temporal resolution, satellite-derived winds,
724 and clear-sky radiances from polar orbiting satellites had an overall positive
725 impact on the development of the studied MCS and its associated precipitation.
726 Moreover, the ensemble forecasts initialized from the analysis show promising
727 results to predict the precipitation of severe events. In the future, we will
728 further analyze the impacts in the independent forecasts and evaluate the

729 implementation of other sources of observations like GPS radio occultation
730 data and radiances from geostationary orbiting satellites.

731 **5. Code and data availability**

732 A version-controlled repository of the code used to create this analysis,
733 including the code used to download the data can be found at <https://github.com/paocorralles/mesoda>. The derived data that support the findings of this
734 study are also openly available in Zenodo at <http://doi.org/10.5072/zenodo.1060834>,
735 version 0.9.0.

737 **Acknowledgements**

738 We are very thankful to the Atmospheric and Sea Research Center (CIMA),
739 the University of Buenos Aires (UBA), and the National Scientific and Tech-
740 nical Research Council (CONICET) who support this study. We acknowledge
741 the Sistema Nacional de Radares Meteorológicos supported by the Secre-
742 taría de Infraestructura y Política Hídrica for kindly providing the radar
743 observations used for validation and the National Meteorological Service
744 for facilitating the access to the data. We also acknowledge the Cheyenne
745 HPC resources (doi:10.5065/D6RX99HX) from NCAR's Computational and
746 Information Systems Laboratory, National Science Foundation (project code
747 UIUC0012). Also, PICT 2017-2233 and PICT 2018-3202 projects of the
748 National Agency for the Promotion of Research, Technological Development
749 and Innovation from Argentina partially funded this project.

750 **References**

- 751 Allaire, J., Horner, J., Xie, Y., Marti, V., Porte, N., 2019. Markdown:
752 Render markdown with the c library 'sundown'.
- 753 Bae, J.-H., Min, K.-H., 2022. Forecast Characteristics of Radar Data
754 Assimilation Based on the Scales of Precipitation Systems. *Remote Sensing*
755 14, 605. doi:10.3390/rs14030605
- 756 Banos, I.H., Mayfield, W.D., Ge, G., Sapucci, L.F., Carley, J.R., Nance,
757 L., 2021. Assessment of the data assimilation framework for the Rapid
758 Refresh Forecast System v0.1 and impacts on forecasts of convective storms.
759 *Geoscientific Model Development Discussions* 1–36. doi:10.5194/gmd-2021-
760 289
- 761 Bao, Y., Xu, J., Powell Jr., A.M., Shao, M., Min, J., Pan, Y., 2015.
762 Impacts of AMSU-A, MHS and IASI data assimilation on temperature and
763 humidity forecasts with GSI–WRF over the western United States. *Atmos.*
764 *Meas. Tech.* 8, 4231–4242. doi:10.5194/amt-8-4231-2015
- 765 Brooks, H.E., Lee, J.W., Craven, J.P., 2003. The spatial distribution of
766 severe thunderstorm and tornado environments from global reanalysis data.
767 *Atmospheric Research* 67–68, 73–94. doi:10.1016/S0169-8095(03)00045-0
- 768 Campitelli, E., 2020. metR: Tools for Easier Analysis of Meteorological
769 Fields.
- 770 Candille, G., Côté, C., Houtekamer, P.L., Pellerin, G., 2007. Verification
771 of an Ensemble Prediction System against Observations. *Mon. Wea. Rev.*
772 135, 2688–2699. doi:10.1175/MWR3414.1
- 773 Cecil, D.J., Blankenship, C.B., 2012. Toward a Global Climatology of
774 Severe Hailstorms as Estimated by Satellite Passive Microwave Imagers.

775 Journal of Climate 25, 687–703. doi:10.1175/JCLI-D-11-00130.1

776 Chang, W., Jacques, D., Fillion, L., Baek, S.-J., 2017. Assimilation of
777 Hourly Surface Observations with the Canadian High-Resolution Ensemble
778 Kalman Filter. Atmosphere-Ocean 55, 247–263. doi:10.1080/07055900.2017.1384361

779 Chen, F., Dudhia, J., 2001. Coupling an Advanced Land Surface–Hydrology
780 Model with the Penn State–NCAR MM5 Modeling System. Part I: Model
781 Implementation and Sensitivity. Monthly Weather Review 129, 569–585.
782 doi:10.1175/1520-0493(2001)129<0569:CAALSH>2.0.CO;2

783 Chen, Q., Fan, J., Hagos, S., Gustafson, W.I., Berg, L.K., 2015. Roles
784 of wind shear at different vertical levels: Cloud system organization and
785 properties. Journal of Geophysical Research: Atmospheres 120, 6551–6574.
786 doi:10.1002/2015JD023253

787 Chen, X., Zhao, K., Sun, J., Zhou, B., Lee, W.-C., 2016. Assimilating
788 surface observations in a four-dimensional variational Doppler radar data
789 assimilation system to improve the analysis and forecast of a squall line case.
790 Adv. Atmos. Sci. 33, 1106–1119. doi:10.1007/s00376-016-5290-0

791 Cherubini, T., Businger, S., Velden, C., Ogasawara, R., 2006. The Impact
792 of Satellite-Derived Atmospheric Motion Vectors on Mesoscale Forecasts over
793 Hawaii. Monthly Weather Review 134, 2009–2020. doi:10.1175/MWR3163.1

794 Clark, A.J., 2017. Generation of Ensemble Mean Precipitation Forecasts
795 from Convection-Allowing Ensembles. Weather and Forecasting 32, 1569–1583.
796 doi:10.1175/WAF-D-16-0199.1

797 Computational and Information Systems Laboratory, 2019. Cheyenne:
798 HPE/SGI ICE XA System (University Community Computing). National
799 Center for Atmospheric Research Boulder, CO. doi:doi:10.5065/D6RX99HX

- 800 de Elía, R., Vidal, L., Lohigorry, P., 2017. El SMN y la red argentina de
801 radares meteorológicos [WWW Document]. URL <http://hdl.handle.net/20.500.12160/625>
- 803 Dillon, M.E., Maldonado, P., Corrales, P., Skabar, Y.G., Ruiz, J., Sacco,
804 M., Cutraro, F., Mingari, L., Matsudo, C., Vidal, L., Rugna, M., Hobouchian,
805 M.P., Salio, P., Nesbitt, S., Saulo, C., Kalnay, E., Miyoshi, T., 2021. A rapid
806 refresh ensemble based data assimilation and forecast system for the RELAM-
807 PAGO field campaign. *Atmospheric Research* 105858. doi:10.1016/j.atmosres.2021.105858
- 808 Dillon, M.E., Skabar, Y.G., Ruiz, J., Kalnay, E., Collini, E.A., Echevarría,
809 P., Saucedo, M., Miyoshi, T., Kunii, M., 2016. Application of the WRF-
810 LETKF Data Assimilation System over Southern South America: Sensitivity
811 to Model Physics. *Wea. Forecasting* 31, 217–236. doi:10.1175/WAF-D-14-
812 00157.1
- 813 Dowle, M., Srinivasan, A., 2020. Data.Table: Extension of 'data.frame'.
- 814 Earth Observing Laboratory, U. -, 2020. Multi-network composite highest
815 resolution radiosonde data. Version 1.3. UCAR/NCAR - earth observing
816 laboratory.
- 817 Eyre, J.R., English, S.J., Forsythe, M., 2020. Assimilation of satellite data
818 in numerical weather prediction. Part I: The early years. *Quarterly Journal
819 of the Royal Meteorological Society* 146, 49–68. doi:10.1002/qj.3654
- 820 Garcia, F., Ruiz, J., Salio, P., Bechis, H., Nesbitt, S., 2019. Argentina
821 mesonet data. Version 1.1. UCAR/NCAR - earth observing laboratory.
- 822 Gasperoni, N.A., Wang, X., Brewster, K.A., Carr, F.H., 2018. Assessing
823 Impacts of the High-Frequency Assimilation of Surface Observations for the
824 Forecast of Convection Initiation on 3 April 2014 within the Dallas–Fort Worth

- 825 Test Bed. Monthly Weather Review 146, 3845–3872. doi:10.1175/MWR-D-
826 18-0177.1
- 827 Goncalves de Goncalves, L.G., Sapucci, L., Vendrasco, E., de Mattos, J.G.,
828 Ferreira, C., Khamis, E., Cruz, N., 2015. A rapid update data assimilation
829 cycle over South America using 3DVar and EnKF, in: The 20th International
830 TOVS Study Conference (ITSC-20). The 20th International TOVS Study
831 Conference (ITSC-20), Lake Geneva, Wisconsin, USA.
- 832 Grell, G.A., Freitas, S.R., 2013. A scale and aerosol aware stochastic
833 convective parameterization for weather and air quality modeling. Atmos.
834 Chem. Phys. Discuss. 13, 23845–23893. doi:10.5194/acpd-13-23845-2013
- 835 Ha, S.-Y., Snyder, C., 2014. Influence of Surface Observations in Mesoscale
836 Data Assimilation Using an Ensemble Kalman Filter. Monthly Weather
837 Review 142, 1489–1508. doi:10.1175/MWR-D-13-00108.1
- 838 Han, Y., Van Delst, P., Liu, Q., Weng, F., Yan, B., Treadon, R., Derber,
839 J., 2006. JCSDA Community Radiative Transfer Model (CRTM)—version 1,
840 NOAA Technical Report NESDIS 122. Washington, D.C.
- 841 Hong, S.-Y., Kim, J.-H., Lim, J.-o., Dudhia, J., 2006. The WRF Single
842 Moment 6-Class Microphysics Scheme (WSM6). Journal of the Korean
843 Meteorological Society 42, 129–151.
- 844 Hong, S.-Y., Noh, Y., Dudhia, J., 2006. A New Vertical Diffusion Package
845 with an Explicit Treatment of Entrainment Processes. Mon. Wea. Rev. 134,
846 2318–2341. doi:10.1175/MWR3199.1
- 847 Hu, M., Ge, G., Zhou, C., Stark, D., Shao, H., Newman, K., Beck, J.,
848 Zhang, X., 2018. Grid-point Statistical Interpolation (GSI) User’s Guide
849 Version 3.7. Developmental Testbed Center.

- 850 Huffman, G., Bolvin, D., Braithwaite, D., Hsu, K., Joyce, R., Kidd, C.,
851 Nelkin, E., Sorooshian, S., Tan, J., Xie, P., 2018. NASA Global Precipitation
852 Measurement (GPM) Integrated Multi-satellitE Retrievals for GPM (IMERG).
853 National Aeronautics and Space Administration (NASA).
- 854 Hunt, B.R., Kostelich, E.J., Szunyogh, I., 2007. Efficient data assimilation
855 for spatiotemporal chaos: A local ensemble transform Kalman filter. Physica
856 D: Nonlinear Phenomena 230, 112–126. doi:10.1016/j.physd.2006.11.008
- 857 Iacono, M.J., Delamere, J.S., Mlawer, E.J., Shephard, M.W., Clough,
858 S.A., Collins, W.D., 2008. Radiative forcing by long-lived greenhouse gases:
859 Calculations with the AER radiative transfer models. J. Geophys. Res. 113,
860 D13103. doi:10.1029/2008JD009944
- 861 Janjić, Z.I., 1994. The Step-Mountain Eta Coordinate Model: Fur-
862 ther Developments of the Convection, Viscous Sublayer, and Turbulence
863 Closure Schemes. Mon. Wea. Rev. 122, 927–945. doi:10.1175/1520-
864 0493(1994)122<0927:TSMECM>2.0.CO;2
- 865 Jones, T.A., Otkin, J.A., Stensrud, D.J., Knopfmeier, K., 2013. Assimila-
866 tion of Satellite Infrared Radiances and Doppler Radar Observations during
867 a Cool Season Observing System Simulation Experiment. Mon. Wea. Rev.
868 141, 3273–3299. doi:10.1175/MWR-D-12-00267.1
- 869 Kain, J.S., 2004. The Kain–Fritsch Convective Parameterization: An
870 Update. JOURNAL OF APPLIED METEOROLOGY 43, 12.
- 871 Lin, H., Weygandt, S.S., Benjamin, S.G., Hu, M., 2017. Satellite Radi-
872 ance Data Assimilation within the Hourly Updated Rapid Refresh. Wea.
873 Forecasting 32, 1273–1287. doi:10.1175/WAF-D-16-0215.1
- 874 Maejima, Y., Miyoshi, T., Kunii, M., Seko, H., Sato, K., 2019. Impact

875 of Dense and Frequent Surface Observations on 1-Minute-Update Severe
876 Rainstorm Prediction: A Simulation Study. Journal of the Meteorological
877 Society of Japan. Ser. II 97, 253–273. doi:10.2151/jmsj.2019-014

878 Maldonado, P., Ruiz, J., Saulo, C., 2021. Sensitivity to Initial and Bound-
879 ary Perturbations in Convective-Scale Ensemble-Based Data Assimilation:
880 Imperfect-Model OSSEs. SOLA 17, 96–102. doi:10.2151/sola.2021-015

881 Mallick, S., Jones, T.A., 2020. Assimilation of GOES-16 satellite derived
882 winds into the warn-on-forecast system. Atmospheric Research 245, 105131.
883 doi:10.1016/j.atmosres.2020.105131

884 Markowski, P., Richardson, Y., 2010. Organization of Isolated Convection,
885 in: Mesoscale Meteorology in Midlatitudes. John Wiley & Sons, Ltd, pp.
886 201–244. doi:10.1002/9780470682104.ch8

887 Matsudo, C., García Skabar, Y., Ruiz, J., Vidal, L., Salio, P., 2015.
888 Verification of WRF-ARW convective-resolving forecasts over Southeastern
889 South America. Mausam 66, 445–456.

890 Nakanishi, M., Niino, H., 2009. Development of an Improved Turbulence
891 Closure Model for the Atmospheric Boundary Layer. JMSJ 87, 895–912.
892 doi:10.2151/jmsj.87.895

893 National Centers for Environmental Prediction, National Weather Service,
894 NOAA, U.S. Department of Commerce, 2015. NCEP GFS 0.25 degree global
895 forecast grids historical archive.

896 Necker, T., Geiss, S., Weissmann, M., Ruiz, J., Miyoshi, T., Lien, G.,
897 2020. A convective-scale 1,000-member ensemble simulation and potential
898 applications. Q.J.R. Meteorol. Soc 146, 1423–1442. doi:10.1002/qj.3744

899 Nesbitt, S.W., Salio, P.V., Ávila, E., Bitzer, P., Carey, L., Chandrasekar,

900 V., Deierling, W., Dominguez, F., Dillon, M.E., Garcia, C.M., Gochis, D.,
901 Goodman, S., Hence, D.A., Kosiba, K.A., Kumjian, M.R., Lang, T., Luna,
902 L.M., Marquis, J., Marshall, R., McMurdie, L.A., Nascimento, E.L., Ras-
903 mussen, K.L., Roberts, R., Rowe, A.K., Ruiz, J.J., Sabbas, E.F.M.T.S., Saulo,
904 A.C., Schumacher, R.S., Skabar, Y.G., Machado, L.A.T., Trapp, R.J., Varble,
905 A., Wilson, J., Wurman, J., Zipser, E.J., Arias, I., Bechis, H., Grover, M.A.,
906 2021. A storm safari in Subtropical South America: Proyecto RELAMPAGO.
907 Bulletin of the American Meteorological Society -1, 1–64. doi:10.1175/BAMS-
908 D-20-0029.1

909 Otsuka, M., Kunii, M., Seko, H., Shimoji, K., Hayashi, M., Yamashita, K.,
910 2015. Assimilation Experiments of MTSAT Rapid Scan Atmospheric Motion
911 Vectors on a Heavy Rainfall Event. Journal of the Meteorological Society of
912 Japan. Ser. II 93, 459–475. doi:10.2151/jmsj.2015-030

913 Ouaraini, R.E., Berre, L., Fischer, C., Sayouty, E.H., 2015. Sensitivity
914 of regional ensemble data assimilation spread to perturbations of lateral
915 boundary conditions. Tellus A: Dynamic Meteorology and Oceanography 67,
916 28502. doi:10.3402/tellusa.v67.28502

917 Rasmussen, K.L., Zuluaga, M.D., Houze, R.A., 2014. Severe convection
918 and lightning in subtropical South America. Geophysical Research Letters
919 41, 7359–7366. doi:10.1002/2014GL061767

920 R Core Team, 2020. R: A language and environment for statistical
921 computing. R Foundation for Statistical Computing, Vienna, Austria.

922 Roberts, B., Gallo, B.T., Jirak, I.L., Clark, A.J., Dowell, D.C., Wang, X.,
923 Wang, Y., 2020. What Does a Convection-Allowing Ensemble of Opportunity
924 Buy Us in Forecasting Thunderstorms? Weather and Forecasting 35, 2293–

- 925 2316. doi:10.1175/WAF-D-20-0069.1
- 926 Roberts, N., 2008. Assessing the spatial and temporal variation in the skill
927 of precipitation forecasts from an NWP model. *Meteorological Applications*
928 15, 163–169. doi:10.1002/met.57
- 929 Ruiz, J.J., Saulo, C., Nogués-Paegle, J., 2010. WRF Model Sensitivity to
930 Choice of Parameterization over South America: Validation against Surface
931 Variables. *Mon. Wea. Rev.* 138, 3342–3355. doi:10.1175/2010MWR3358.1
- 932 Sawada, M., Ma, Z., Mehra, A., Tallapragada, V., Oyama, R., Shimoji, K.,
933 2019. Impacts of Assimilating High-Resolution Atmospheric Motion Vectors
934 Derived from Himawari-8 on Tropical Cyclone Forecast in HWRF. *Monthly*
935 *Weather Review* 147, 3721–3740. doi:10.1175/MWR-D-18-0261.1
- 936 Shao, H., Derber, J., Huang, X.-Y., Hu, M., Newman, K., Stark, D.,
937 Lueken, M., Zhou, C., Nance, L., Kuo, Y.-H., Brown, B., 2016. Bridging
938 Research to Operations Transitions: Status and Plans of Community GSI. *Bul-*
939 *letin of the American Meteorological Society* 97, 1427–1440. doi:10.1175/BAMS-
940 D-13-00245.1
- 941 Singh, R., Ojha, S.P., Kishtawal, C.M., Pal, P.K., Kiran Kumar, A.S.,
942 2016. Impact of the assimilation of INSAT-3D radiances on short-range
943 weather forecasts: Assimilation of INSAT-3D Radiances. *Q.J.R. Meteorol.*
944 *Soc.* 142, 120–131. doi:10.1002/qj.2636
- 945 Skamarock, W.C., Klemp, J.B., Dudhia, J., Gill, D.O., Barker, D.M.,
946 Duda, M.G., Huang, X.-Y., Wang, W., Powers, J.G., 2008. A Description of
947 the Advanced Research WRF Version 3.
- 948 Sobash, R.A., Stensrud, D.J., 2015. Assimilating Surface Mesonet Ob-
949 servations with the EnKF to Improve Ensemble Forecasts of Convection

- 950 Initiation on 29 May 2012. *Monthly Weather Review* 143, 3700–3725.
951 doi:10.1175/MWR-D-14-00126.1
- 952 Sun, J., Xue, M., Wilson, J.W., Zawadzki, I., Ballard, S.P., Onvlee-
953 Hooimeyer, J., Joe, P., Barker, D.M., Li, P.-W., Golding, B., Xu, M., Pinto,
954 J., 2014. Use of NWP for Nowcasting Convective Precipitation: Recent
955 Progress and Challenges. *Bulletin of the American Meteorological Society* 95,
956 409–426. doi:10.1175/BAMS-D-11-00263.1
- 957 Wang, Z.Q., Randriamampianina, R., 2021. The Impact of Assimilat-
958 ing Satellite Radiance Observations in the Copernicus European Regional
959 Reanalysis (CERRA). *Remote Sensing* 13, 426. doi:10.3390/rs13030426
- 960 Weston, P., Geer, A., Bormann, N., Bormann, N., 2019. Investigations
961 into the assimilation of AMSU-A in the presence of cloud and precipitation
962 [WWW Document]. EUMETSAT/ECMWF Fellowship Programme Research
963 Report. doi:10.21957/ewahn9ce
- 964 Wheatley, D.M., Stensrud, D.J., 2010. The Impact of Assimilating Surface
965 Pressure Observations on Severe Weather Events in a WRF Mesoscale Ensem-
966 ble System. *Monthly Weather Review* 138, 1673–1694. doi:10.1175/2009MWR3042.1
- 967 Whitaker, J.S., Hamill, T.M., 2012. Evaluating Methods to Account
968 for System Errors in Ensemble Data Assimilation. *Mon. Wea. Rev.* 140,
969 3078–3089. doi:10.1175/MWR-D-11-00276.1
- 970 Wickham, H., 2009. *Ggplot2: Elegant Graphics for Data Analysis*, Use
971 R! Springer-Verlag, New York. doi:10.1007/978-0-387-98141-3
- 972 Wu, T.-C., Liu, H., Majumdar, S.J., Velden, C.S., Anderson, J.L., 2014.
973 Influence of Assimilating Satellite-Derived Atmospheric Motion Vector Ob-
974 servations on Numerical Analyses and Forecasts of Tropical Cyclone Track

- 975 and Intensity. Monthly Weather Review 142, 49–71. doi:10.1175/MWR-D-
976 13-00023.1
- 977 Xie, Y., 2015. Dynamic documents with R and knitr, Second. ed. Chap-
978 man and Hall/CRC, Boca Raton, Florida.
- 979 Zhao, J., Gao, J., Jones, T.A., Hu, J., 2021a. Impact of Assimilating High-
980 Resolution Atmospheric Motion Vectors on Convective Scale Short-Term Fore-
981 casts: 1. Observing System Simulation Experiment (OSSE). Journal of Ad-
982 vances in Modeling Earth Systems 13, e2021MS002484. doi:10.1029/2021MS002484
- 983 Zhao, J., Gao, J., Jones, T.A., Hu, J., 2021b. Impact of Assimilating
984 High-Resolution Atmospheric Motion Vectors on Convective Scale Short-
985 Term Forecasts: 2. Assimilation Experiments of GOES-16 Satellite Derived
986 Winds. Journal of Advances in Modeling Earth Systems 13, e2021MS002486.
987 doi:10.1029/2021MS002486
- 988 Zhu, K., Xue, M., Pan, Y., Hu, M., Benjamin, S.G., Weygandt, S.S.,
989 Lin, H., 2019. The Impact of Satellite Radiance Data Assimilation within a
990 Frequently Updated Regional Forecast System Using a GSI-based Ensemble
991 Kalman Filter. Adv. Atmos. Sci. 36, 1308–1326. doi:10.1007/s00376-019-
992 9011-3
- 993 Zhu, Y., Derber, J., Collard, A., Dee, D., Treadon, R., Gayno, G., Jung,
994 J.A., 2014. Enhanced radiance bias correction in the National Centers for
995 Environmental Prediction’s Gridpoint Statistical Interpolation data assim-
996 ilation system. Quarterly Journal of the Royal Meteorological Society 140,
997 1479–1492. doi:10.1002/qj.2233
- 998 Zhu, Y., Liu, E., Mahajan, R., Thomas, C., Groff, D., Van Delst, P.,
999 Collard, A., Kleist, D., Treadon, R., Derber, J.C., 2016. All-Sky Microwave

₁₀₀₀ Radiance Assimilation in NCEP's GSI Analysis System. Mon. Wea. Rev.
₁₀₀₁ 144, 4709–4735. doi:10.1175/MWR-D-15-0445.1

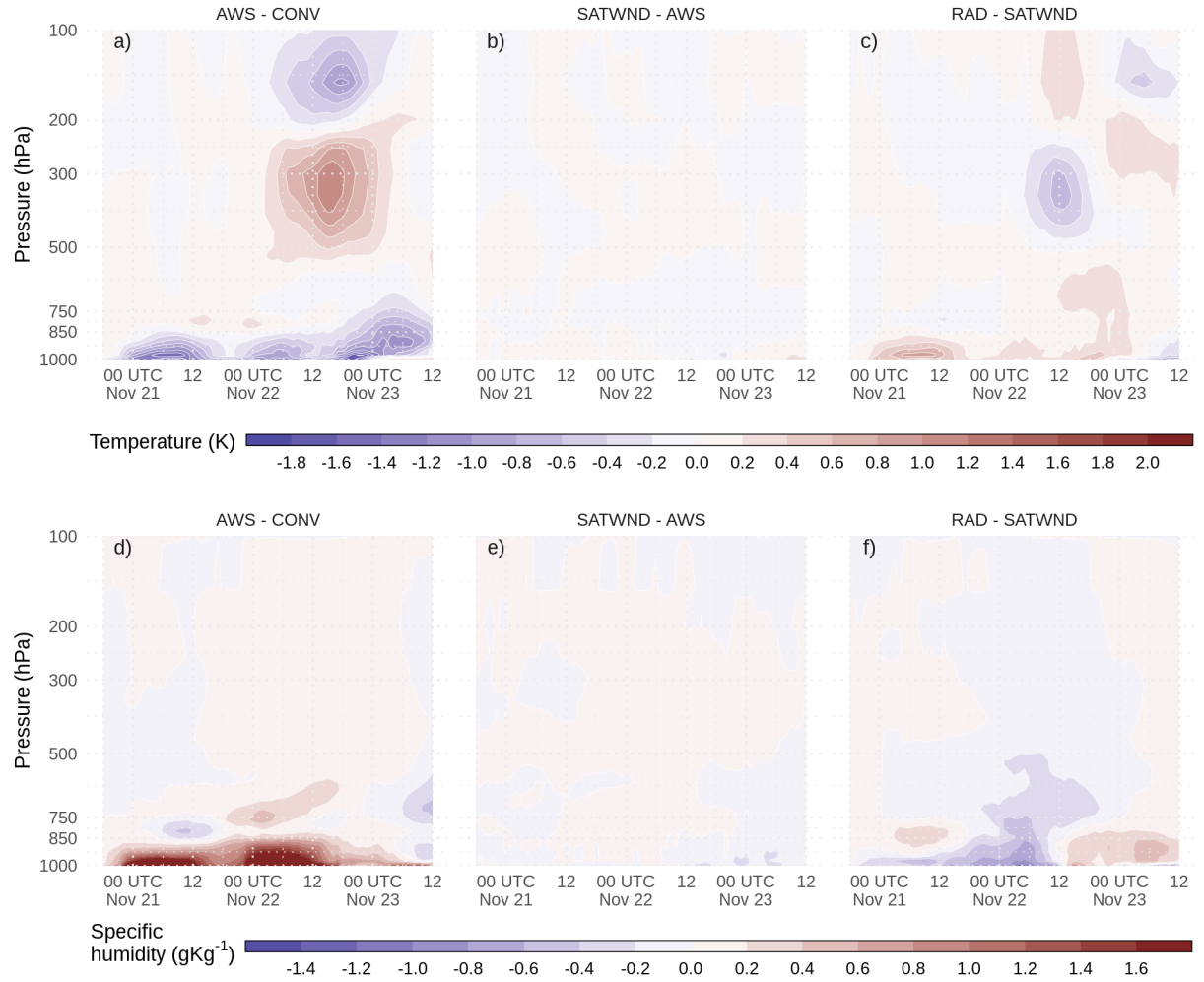


Figure 7: Difference between analysis ensemble mean experiments a) and d) AWS-CONV, b) and e) SATWND-AWS, and c) and f) RAD-SATWND for the spatially averaged vertical profiles of temperature (a, b, and c, in K) and specific humidity (d, e, and f in gkg^{-1}) calculated over the inner domain (red box in Figure 1a) for each analysis cycle.

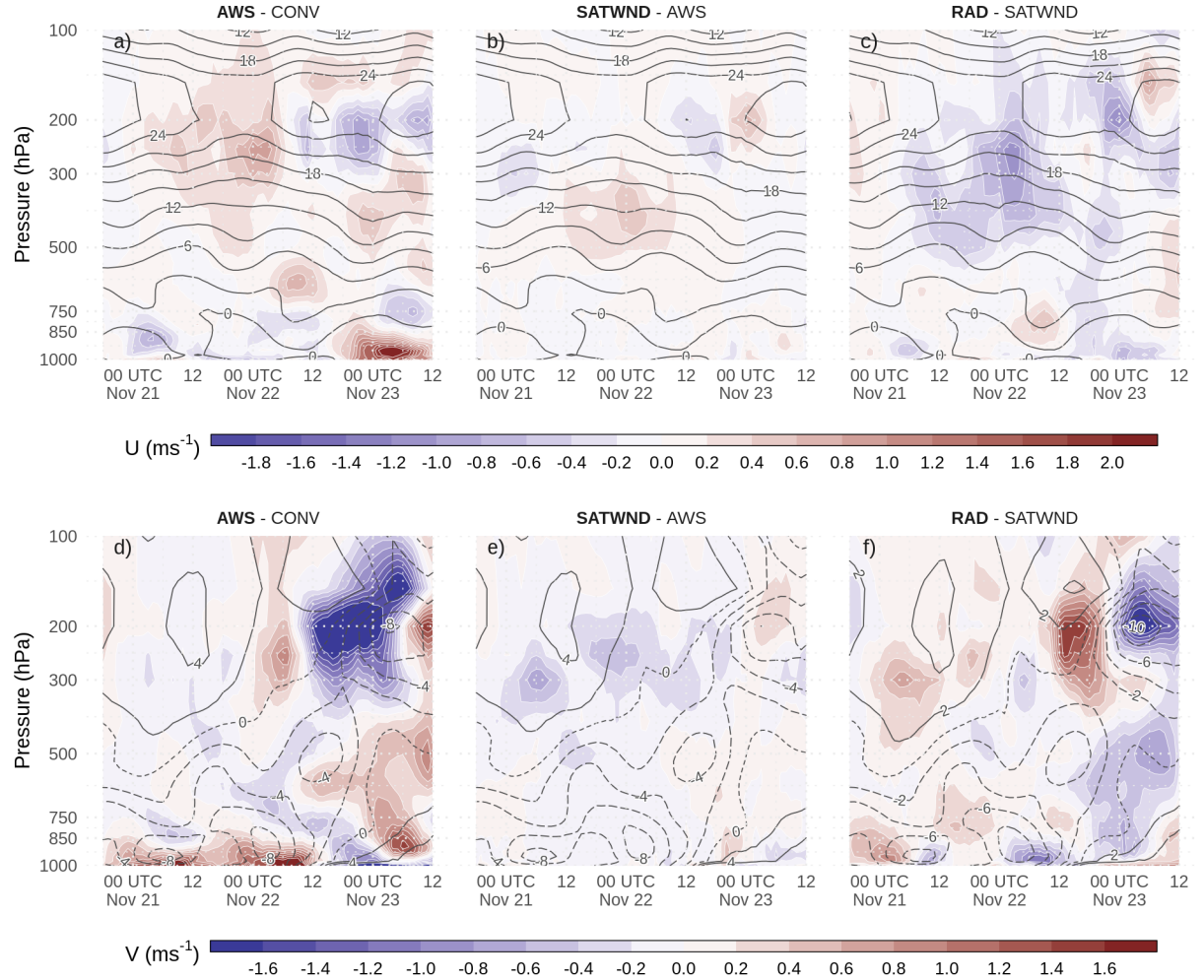


Figure 8: Difference between analysis ensemble mean experiments a) and d) AWS-CONV, b) and e) SATWND-AWS, and c) and f) RAD-SATWND for the spatially averaged vertical profiles of u wind (a, b, and c, in ms^{-1}) and v wind (d, e, and f in ms^{-1}) calculated over the inner domain (red box in Figure 1a) for each analysis cycle. Black contours correspond to negative u wind for (a) AWS, (b) SATWND, and (c) RAD and v wind for (d) AWS, (e) SATWND, and (f) RAD. Dashed contours correspond to negative v wind.

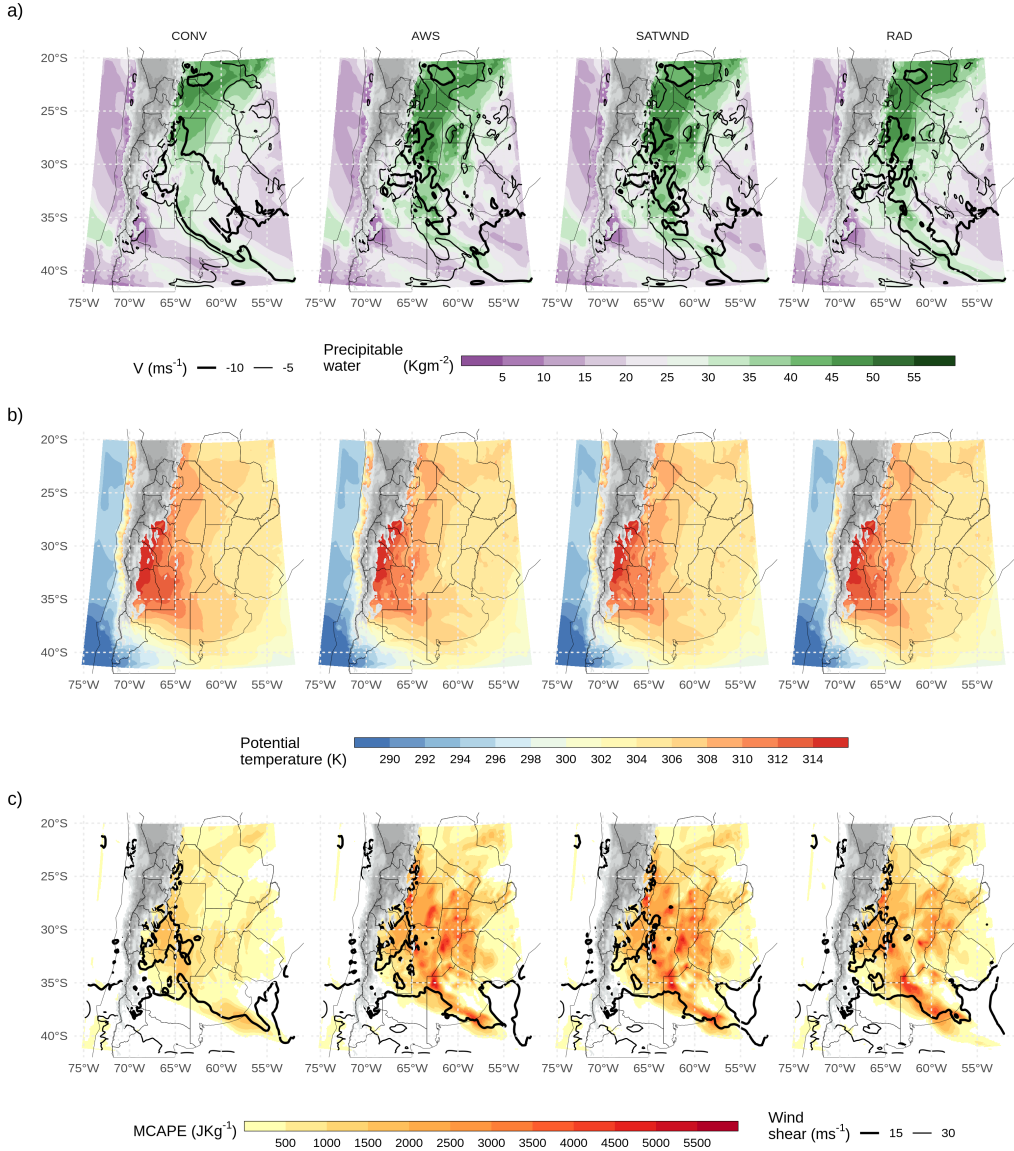


Figure 9: a) Precipitable water (shaded, kgm^{-2}) and average northerly wind over the first 7 sigma levels (from the surface up to approximately 800 hPa, contours, ms^{-1}), b) Average potential temperature for the PBL (first 10 sigma levels), and c) Maximum CAPE and $\sim 0\text{-}6$ km wind shear over 15 and 30 ms^{-1} for each experiment. All fields correspond to the analysis ensemble mean for 00 UTC Nov 22. Grey filled contours correspond to topography over 1500 meters above sea level.

54

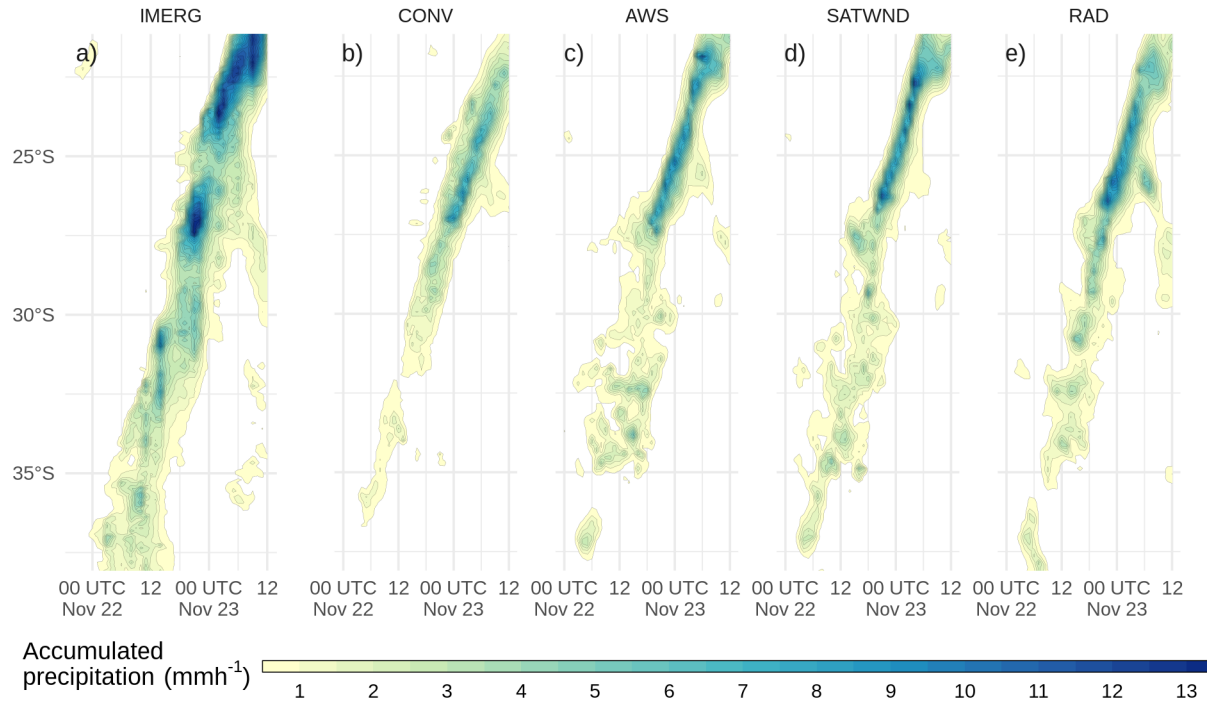


Figure 10: Hövmoller diagram of probability matched mean hourly accumulated 1-h forecast precipitation for each latitude band estimated by IMERG (left) and simulated (right), for the ensemble mean of each experiment, averaged over a longitude range between 67°W and 54.5°W . Contours drawn every 0.5 mmh^{-1} , starting at 0.5 mmh^{-1} .

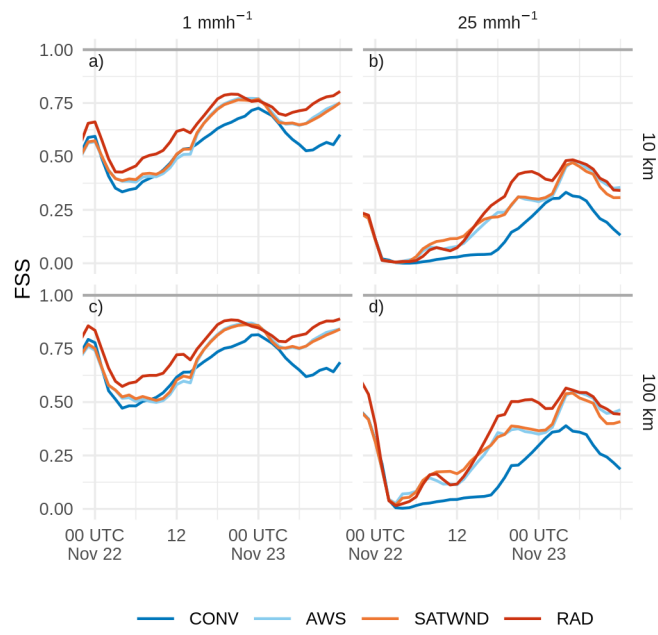


Figure 11: FSS calculated over 1-h forecast precipitation accumulated in a 6-hour moving window for 1 mm (a and c) and 25 mm (b and d) thresholds, on 10 km (a and b) and 100 km (c and d) scales, for the first-guess of CONV (blue line), AWS (light blue line), SATWND (orange line) and RAD (red line) experiments.

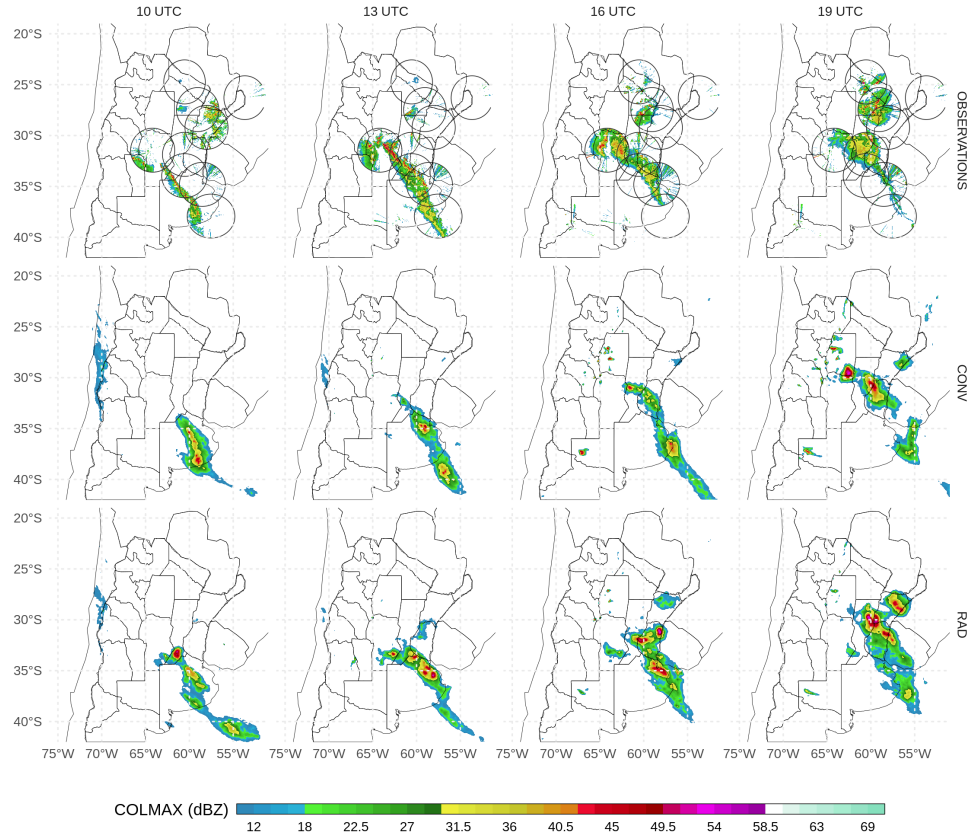


Figure 12: Maximum reflectivity in the column (COLMAX in dBZ), observed (upper row) and 1-hr forecast probability matched mean column maximum reflectivity for CONV (second row) and RAD (third row) at 10 UTC (first column), 13 UTC (second column), 16 UTC (third column), and 19 UTC (fourth column) Nov 22, 2018. Black circles in first row show the observation range of each radar.

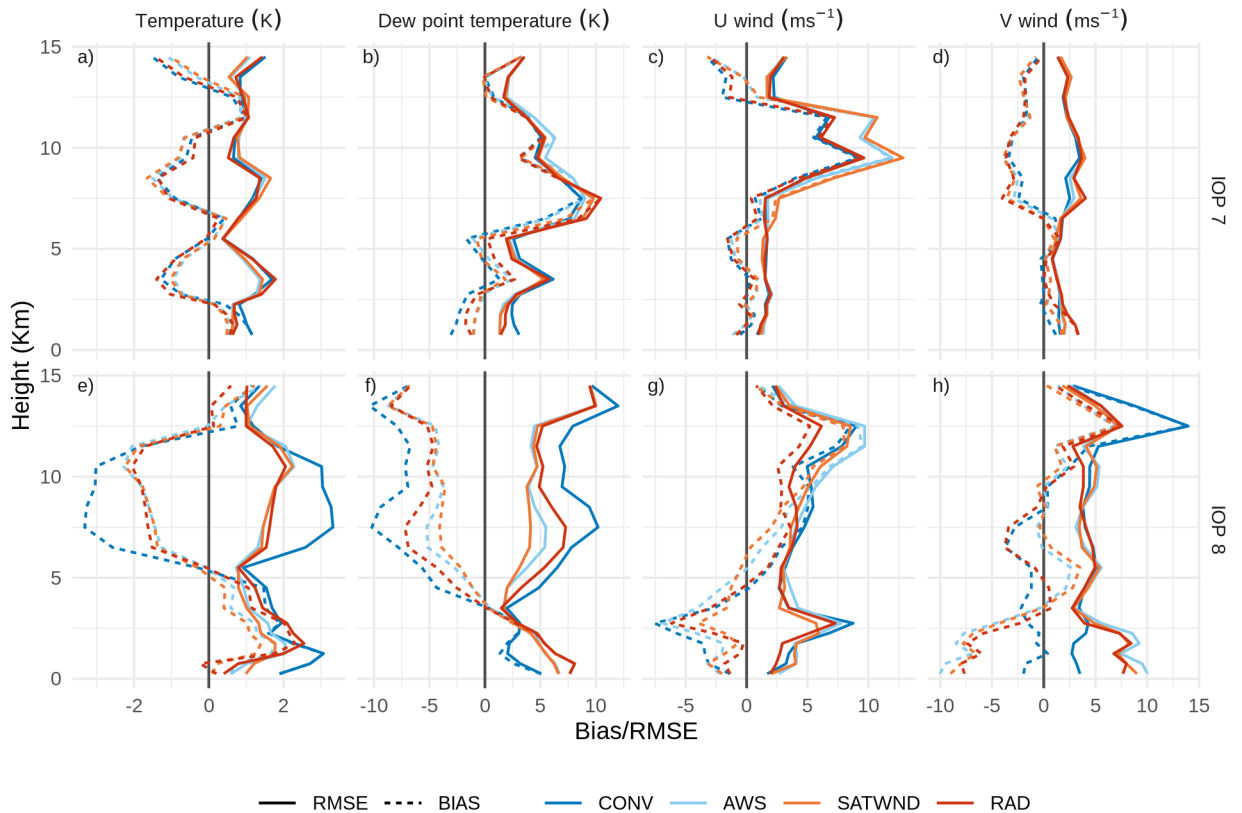


Figure 13: RMSE (solid line) and Bias (dashed line) of a) temperature (K), b) dew point temperature (K), c) u wind ($m s^{-1}$) and d) v wind ($m s^{-1}$) calculated by comparing the analysis of each experiment with the RELAMPAGO soundings during IOP 7 and IOP 8. The blue line corresponds to CONV, the light blue line to AWS, SATWND is represented with an orange line, and RAD with a red line.

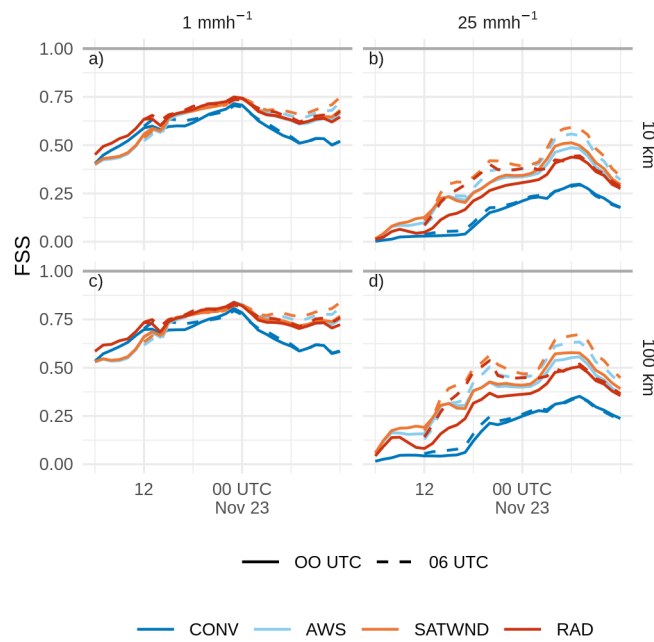


Figure 14: FSS calculated over a 6-hour moving window for 1 mm (a and c) and 25 mm (b and d) thresholds, on 10 km (a and b) and 100 km (c and d) scales, for the forecasts initialized from CONV (blue line), AWS (light blue line), SATWND (orange line), and RAD (red line) experiments at 00 UTC (solid line) and 06 UTC (dashed line), Nov 22.